Redox Biology 91 (2026) 104068

Contents lists available at ScienceDirect

Redox Biology

journal homepage: www.elsevier.com/locate/redox

NRF2 deficit prevents pathologic Tau seeding and spreading in an induced tauopathy mouse model

Yaiza López-Sampere [a,b], Pol Mengod Soler [a,b], Sergio Roca-Pereira [a,b], Antonia Vinyals [a,b], Xoel Mato-Blanco [c], Marta Vela-Martínez [a,b], Farida Dakterzada [d], Leila Romero [d], Enrique Santamaría [e], Joaquín Fernández-Irigoyen [e], Isidro Ferrer [f], Mónica Povedano [a,b,g], José Antonio Del Rio [b,h,i,j], Gabriel Santpere [c], Manuel Portero-Otín [k], Gerard Piñol-Ripoll [d,*,1], Pol Andrés-Benito [b,d,h,**,1]

[a] Neurology and Neurogenetics Group - Neuroscience Program, Bellvitge Biomedical Research Institute (IDIBELL), L'Hospitalet de Llobregat, Barcelona, 08907, Spain
[b] Network Centre of Biomedical Research of Neurodegenerative Diseases (CIBERNED), Institute of Health Carlos III, L'Hospitalet de Llobregat, Barcelona, 08907, Spain
[c] Neurogenomics Group, Hospital del Mar Research Institute, Parc de Recerca Biomèdica de Barcelona (PRBB), Dr. Aiguader, 88, Barcelona, Catalonia, 08003, Spain
[d] Cognition and Behaviour Study Group – Institute for Research in Biomedicine of Lleida (IRBLleida), Lleida, 25196, Spain
[e] Proteomics Unit, Clinical Neuroproteomics Laboratory, Navarrabiomed, Hospital Universitario de Navarra (HUN), Universidad Pública de Navarra (UPNA), Instituto de Investigación Sanitaria de Navarra (IdiSNA)., Pamplona, Navarra, 31008, Spain
[f] Department of Pathology and Experimental Therapeutics – Bellvitge Faculty, University of Barcelona, L'Hospitalet de Llobregat, Barcelona, 08907, Spain
[g] Functional Unit of Amyotrophic Lateral Sclerosis (UFELA), Service of Neurology, Bellvitge University Hospital, L'Hospitalet de Llobregat, Barcelona, 08907, Spain
[h] Molecular and Cellular Neurobiotechnology, Institute for Bioengineering of Catalonia (IBEC), Barcelona Institute of Science and Technology (BIST), Science Park of Barcelona, Barcelona, 08028, Spain
[i] Institute of Neurosciences, University of Barcelona, Barcelona, Spain
[j] Department of Cell Biology, Physiology and Immunology, Faculty of Biology, University of Barcelona, Barcelona, 08028, Spain
[k] Metabolic Pathophysiology Research Group, Department of Experimental Medicine, University of Lleida - Institute for Research in Biomedicine of Lleida (IRBLleida), Lleida, 25196, Spain

ARTICLE INFO

Keywords:
Aging
Alzheimer's disease
NRF2
Oxidative stress
Tau

ABSTRACT

Background: Nuclear factor erythroid 2–related factor 2 (NRF2) regulates antioxidant defenses and protects against neurodegeneration, including Alzheimer's disease (AD). Its age-related decline disrupts redox balance and increases neuronal vulnerability, but the early hippocampal effects remain unclear. Here, we tested whether NRF2 loss affects tau seeding and spreading in a PHF-tau–inoculated mouse model, contributing to accelerated aging.

Methodology: Three-month-old NRF2-knockout (*Nfe2l2*$^{-/-}$) and wild-type (WT) mice received hippocampal inoculations of human AD-derived PHF-tau, and tau propagation was analyzed after three months. To elucidate the molecular underpinnings of the observed changes, we performed integrative phosphoproteotranscriptomic analyses of hippocampal tissue, supported by RT-qPCR and Western blot validation.

Results: PHF-tau inoculation at 3 months of age in *Nfe2l2*$^{-/-}$ mice, surprisingly, exhibited markedly reduced tau seeding and spreading compared to WT after 3 months of incubation. Molecular characterization of the *Nfe2l2*$^{-/-}$ hippocampus was carried out to unravel the molecular changes associated with impaired tau propagation. Transcriptomic profiling revealed 745 deregulated genes in *Nfe2l2*$^{-/-}$ mice, characterized by upregulation of immune and metabolic pathways but downregulation of oxidative stress and redox-related genes. RT-qPCR confirmed diminished expression of antioxidant enzymes and anti-inflammatory receptors, alongside altered astrocytic markers. Proteomic analysis identified 157 dysregulated proteins associated with mitochondrial, synaptic, and inflammatory processes, while phosphoproteomics detected 824 altered phosphosites enriched in cytoskeletal and synaptic networks. Western blot showed increased GFAP-C-term, AQP4, 8-OHdG, and MDAL,

---

* Corresponding author.

** Corresponding author. Cognition and Behaviour Study Group – Institute for Research in Biomedicine of Lleida (IRBLleida), Avinguda Alcalde Rovira Roure 80, 25196, Lleida, Spain.

E-mail addresses: gerard_437302@hotmail.com (G. Piñol-Ripoll), pol.andres.benito@gmail.com (P. Andrés-Benito).

[1] Both authors contributed equally to this work.

https://doi.org/10.1016/j.redox.2026.104068
Received 11 January 2026; Accepted 2 February 2026

with reduced GSTM2 expression. Notably, total and 4R-tau levels were decreased, while 3R-tau was elevated in *Nfe2l2*$^{-/-}$ mice.

Conclusion: Our findings suggest that NRF2 loss induces a hippocampal state marked by impaired antioxidant defenses, astrocytic remodeling, and disrupted tau isoform balance. This environment, while metabolically altered, paradoxically hinders tau propagation, highlighting NRF2 as a key regulator of both redox and cellular maturity programs essential for tau spread and as a potential therapeutic target in tauopathies.

1. Introduction

Oxidative stress is a central factor among the key features collectively known as the “hallmarks of aging,” as it disrupts proteostasis, compromises genomic stability, and induces cell death [1]. Mechanistically, reactive oxygen species (ROS) modulate cellular functions by modifying proteins, lipids, carbohydrates, and nucleic acids, thereby affecting their stability and function. When these ROS are not effectively eliminated, their accumulation leads to oxidative stress, which contributes to pathogenesis. This is particularly significant in the context of aging, where the buildup of oxidative stress is a key driver that increases susceptibility to age-related pathologies, such as neurodegenerative disorders [2]. This heightened susceptibility is partly due to ROS-induced damage to critical intracellular components, which affects the cell's overall redox balance, metabolism, and protein homeostasis [3]. These faults lead to progressive decline in physiological functions contributing to their ageing-related deterioration and increasing vulnerability to damage and disease [4]. These changes contribute to the onset of age-related conditions, including cardiovascular disease, musculoskeletal disorders such as arthritis, cancer, and neurodegenerative diseases like Alzheimer's disease (AD) [4].

One of the defense mechanisms against oxidative stress as well as other cellular stressors is the activation of the nuclear factor (erythroid-derived 2)-like 2 (NRF2) pathways [5]. NRF2 is a transcription factor that regulates the expression of a vast number of genes by binding to the antioxidant response element (ARE) in their promoters. While NRF2 is considered a master regulator of the cellular redox status, it also controls the expression of genes involved in the overall metabolic reprogramming during stress and inflammation [2,6]. Under physiological conditions, NRF2 is kept in the cytosol by its repressor, Kelch-like ECH associating protein 1 (Keap1) [7]. Under oxidative stress or other disturbance in cellular homeostasis, NRF2 is translocated to the nucleus, promotes the expression of crucial genes responsible for detoxification, antioxidant and anti-inflammatory genes, and orchestrates the protective response [8].

During normal aging, NRF2 activity and the expression of its downstream target genes tend to decline across various organs, including the brain [9]. This reduction has been documented in several studies [10,11]. As NRF2 function diminishes with age, the balance between oxidants and antioxidants becomes disrupted, promoting oxidative stress and related cellular damage in the brain and other organs. This is reinforced in pathological conditions such as Hutchinson–Gilford progeria syndrome (HGPS), a rare fatal genetic disorder causing accelerated aging in children, caused by the constitutive production of progerin, a mutant form of the nuclear architectural protein lamin A. In HGPS, progerin sequesters NRF2 and thereby causes its subnuclear mislocalization, resulting in impaired NRF2 transcriptional activity and consequently increased chronic oxidative stress [12].

Several mechanisms have been proposed to explain the age-associated drop in NRF2 signaling; these include reduced expression of NRF2 activators such as PI3K, p62, and CBP; elevated levels of inhibitors like KEAP1 and BACH1; and an overall decline in NRF2 protein levels itself [13–15]. Functionally, this decline in NRF2 activity contributes to lower glutathione (GSH) content, diminished activity of GSH-dependent and antioxidant enzymes, and increased mitochondrial generation of superoxide radicals in the aging brain [16,17]. Nonetheless, human studies demonstrate a strong link between elevated oxidative stress and cognitive decline in older adults [18–20].

Over the years, a strong link has been established between NRF2 function and brain health. This transcription factor plays a critical neuroprotective role in various neurological disorders and brain injuries. Research using animal models has demonstrated that the absence of NRF2 increases vulnerability to inflammatory responses, cellular toxicity, genetic damage, and neurotoxicity triggered by both internal and external stressors related to aging [21–23]. As expected, NRF2 deficiency in mice results in phenotypes that resemble accelerated aging, including enhanced neuroinflammation, oxidative stress induced by obesity, breakdown of the blood-brain barrier, and cognitive impairments [24]. These findings from animal studies have been further supported by clinical observations, with emerging evidence from human research, pointing to a disrupted NRF2 pathway in conditions such as neuroinflammation and neurodegenerative diseases [25–27]. Such insights suggest that modulating NRF2 activity could be a promising therapeutic avenue for age-related brain disorders.

Therefore, understanding the molecular landscape of NRF2 knockout models (*Nfe2l2*$^{-/-}$) provides critical insights into the mechanisms underlying oxidative stress, inflammation, and neurodegeneration. Despite the well-established role of NRF2 as a master regulator of antioxidant defense, comprehensive -omics analyses in *Nfe2l2*$^{-/-}$ animals remain limited. Few studies have examined these changes within specific using omics approaches [28], an none of them focused on specific brain regions where the impact of NRF2 loss may vary depending on local cellular composition and metabolic demands—and neither have investigated these effects during early age stages, as most research has focused on aging-related outcomes [28] or on mixed genetic models for neurological disorders [29–31]. Also, limited studies are present for the potential role of NRF2 loss during early development. During early brain development, rapid synaptogenesis imposes substantial metabolic demands that require adaptive responses in neuronal energy metabolism [32–34].

Our work aims to provide novel insights into early, region-specific molecular changes and to highlight key pathways disrupted by NRF2 deficiency, particularly in how these alterations modulate the seeding and spreading mechanisms of pathological tau in a “sporadic tauopathy” mouse model inoculated in the hippocampus. We focused on the hippocampus because it has been previously explored by our group using three-month-old WT, mutant tau, or humanized tau mouse models [35–39]; in addition to this region is particularly vulnerable to NRF2 deficiency due to its high expression of NRF2 in hippocampal cells; and because of its central role in learning and memory (sustained by earlier synaptogenesis), its high metabolic demand, and its known susceptibility to oxidative damage [40]. Moreover, the hippocampus is among the earliest and most severely affected regions in AD and other age-related tauopathies, making it a key target for investigating early pathogenic mechanisms [41]. Thus, based on the obtained results, we proposed to fully characterize the molecular alterations by generating a detailed phosphoproteotranscriptomic profile of the hippocampus, thereby improving our understanding of NRF2's involvement in tau protein seeding and spreading, as well as its role in aging.

2. Materials and methods

2.1. Human brain samples

Brain samples of the hippocampus were obtained from the Institute of Neuropathology Brain Bank, Bellvitge University Hospital, following the guidelines of the Spanish legislation on this matter (Real Decreto Biobancos 1716/2011) and the approval of the local ethics committee of Bellvitge University Hospital. The agonal state was short, with no evidence of acidosis or prolonged hypoxia; the pH values of the brain samples were between 6.8 and 7. At the time of autopsy, one hemisphere was fixed in paraformaldehyde for no less than 3 weeks, and selected brain sections were embedded in paraffin. De-waxed paraffin sections, 4 μm thick, were processed via neuropathological and immunohistochemical methods. The other hemisphere was cut into coronal sections 1 cm thick, and selected brain regions were dissected, placed in labeled plastic bags, and stored at −80 °C until use. The brain samples used in this study were frozen hippocampus samples from an AD case, a 68-year-old man, Braak and Braak NFT stage V–VI, Braak β-amyloid stage C, Thal phase 4, and CERAD 3, and one age-matched control case (65-year-old man) with no lesions (Braak 0/0, Thal 0; CERAD 0); both of them previously used in other similar experiments [35,37,42]. All these cases did not show co-morbidities; in particular, argyrophilic grains, thorn-shaped astrocytes, coiled bodies, and other tauopathies were absent. Deposits of α-synuclein and TDP43 were not observed in any region.

2.2. Extraction of sarkosyl-insoluble fractions and western blotting from human brain samples

Frozen samples of the hippocampus of about 1 g were lysed in 10 vol (w/v) with cold suspension buffer (10 mM Tris-HCl, pH 7.4, 0.8 M NaCl, 1 mM EGTA) supplemented with 10% sucrose, protease, and phosphatase inhibitors (Roche). The homogenates were first centrifuged at 20,000×*g* for 20 min (Ultracentrifuge Beckman with 70 Ti rotor), and the supernatant (S1) was saved. The pellet was re-homogenized in five volumes of homogenization buffer and re-centrifuged at 20,000×*g* for 20 min. The two supernatants (S1 + S2) were mixed and incubated with 0.1% N-lauroylsarkosynate (sarkosyl) for 1 h while being shaken. Samples were then centrifuged at 100,000×*g* for 1 h. Sarkosyl-insoluble pellets (P3) were re-suspended (0.2 mL/g) in 50 mM Tris-HCl (pH 7.4). Sarkosyl-insoluble fractions were processed for Western blotting, as detailed elsewhere [35]. Western blot confirmation of tau content was performed using an anti-p-Tau-Ser422 antibody (1:2000; Ref. No. 44764G, Thermo Scientific, Waltham, MA, USA) to assess the full banding pattern of the PHF-insoluble fraction, as previously described [35–39,42].

2.3. Animals

All animal procedures were carried out following the guidelines of the European Communities Council Directive 2010/63/EU and with the approval of the local ethical committee (CEEA, Comitè Ètic d'Experimentació Animal; University of Barcelona, Barcelona, Spain; ref. 426/18).

The animals used for this experiment were C57BL/6 mice as wild-type (WT) model and B6.129X1-Nfe2l2tm1Ywk/J, as a NRF2 knockout mice (*Nfe2l2*$^{-/-}$) (strain: #017009) (Jackson Laboratory; Bar Harbor, ME, USA). In this NRF2 knockout strain, a β-galactosidase (*lacZ*) reporter followed by a neomycin resistance (neo) cassette replaces exon 5 and part of exon 4 encoding the nuclear factor, erythroid derived 2, like 2 gene (*Nfe2l2*) gene, abolishing gene expression and its function. Animals were maintained under standard animal housing conditions in a 12 h dark-light cycle, with free access to food and water. Separate cohorts were used due to animal availability, ensuring adequate sample sizes and avoiding confounds from prior testing.

For animal model baseline cognitive performance characterization, we used two-object recognition test in twelve WT and thirteen *Nfe2l2*$^{-/-}$ animals aged 3 months. This paradigm consists of placing the animals for 9 min in a V-maze containing two identical objects at the ends of the arms. Twenty-four hours after the training session, the animals are placed in the V-maze where one of the two familiar objects is replaced by a novel object. The time that the animals spend exploring the two objects is recorded in the training and test sessions; the object Recognition Index (RI) is calculated as the difference between the time spent exploring the novel (TN) and the familiar object (TF) during the test session, divided by the total time spent exploring the two objects [RI = (TN − TF)/(TN + TF)]. Animals exhibiting memory impairments revealed a lower object RI. Investigators in charge of the experiments were blinded to the genomic background of the mice.

For seeding and spreading studies, seven WT and eleven *Nfe2l2*$^{-/-}$ animals aged 3 months were deeply anesthetized using oral isoflurane administration connected to the stereotaxic frame. After assuring lack of reflexes, we performed the intra-hippocampal inoculation of control and AD PHFs extracted fractions, including vehicle extraction buffer, using a Hamilton syringe (volume 2.0 μL); the coordinates were −1.9 mm interaural, +1.4 mm relative to bregma, and −1.8 mm DV from the dural surface [43]. A volume of 1.5 μL was injected at a rate of 0.15 μL/min. The syringe withdrawn slowly over 10 min to avoid leakage of the inoculum.

Following inoculation, the animals were kept in a warm blanket and monitored until they recovered from the anesthesia. Buprenorfina analgesia was administered immediately after surgery and once a day during the next 2 consecutive days. Animals were housed individually with full access to food and water, and they were euthanized by decapitation at the age of 6 months (3 months after inoculation). The brains were rapidly fixed with 4% paraformaldehyde in phosphate buffer and embedded in paraffin.

For animal model characterization, animals were euthanized by decapitation using a rodent guillotine. Animals were minimally handled prior to the procedure to reduce stress. Decapitation was carried out swiftly and without prior anesthesia, as recommended by the institutional ethics committee in cases where anesthetics may alter subsequent biochemical or molecular analyses. Immediately following decapitation, the tissues of interest were rapidly extracted for further studies. The left cerebral hemisphere was dissected on ice-chilled plates into different regions for storage. These tissue samples were immediately frozen and stored at −80 °C until biochemical analyses were performed. The right hemisphere was fixed in 4% phosphate buffered paraformaldehyde (PFA), embedded in paraffin after sectioning into coronal slices, and later used for immunohistochemistry. For -omic approaches and validations, each experimental group consisted of six animals (n = 6), with equal distribution of males and females (3:3). The sample size was determined based on previously published work in comparable models [44,45], and pragmatic considerations typical of exploratory -omics experiments. This group size is sufficient to detect large effect sizes, while findings from -omic analyses were considered hypothesis-generating and validated in independent experiments. This number was therefore sufficient to ensure statistical reliability while minimizing unnecessary animal use. In accordance with the 3Rs principle (Replacement, Reduction, and Refinement), we selected the smallest number of animals required to achieve valid statistical comparisons. The chosen group size represents a balance between ethical responsibility to reduce animal use and the scientific necessity of ensuring reproducible, biologically meaningful results.

2.4. Immunohistochemistry (IHC) in the hippocampus of inoculated *Nfe2l2*$^{-/-}$ and WT animals

To evaluate seeding and spreading potential of human tau in inoculated *Nfe2l2*$^{-/-}$ and WT, de-waxed sections, 4 μm thick, from *Nfe2l2*$^{-/-}$ and WT inoculated animals (3 months post inoculum), seven WT animals and eleven *Nfe2l2*$^{-/-}$ animals, were processed for immunohistochemistry. Sections were boiled in citrate buffer for 20 min to retrieve protein antigenicity. Next, preparations were incubated with Dako REAL Peroxidase-Blocking Solution (Dako, CA, USA) for 15 min to block endogenous peroxidases. Once they are blocked, sections were incubated with the primary antibodies against tau AT8 P-Ser202/Thr205 (Ms, dil. 1:50, Innogenetics, Gante, Belgium). They were diluted in Dako Real Antibody Diluent (Dako, CA, USA). Next day, samples were incubated with a secondary antibody preparation Biotinylated Goat anti-Mouse and Rabbit IgG (H + L) (Abcam, ab64257, Cambridge, UK). After this, samples were incubated with streptavidin using Streptavidin Peroxidase (Abcam, ab64269, Cambridge, UK) for 20 min. Peroxidase activity was developed with 0.03% 3-3′-diaminobenzidine (DAB) and 0.01% H_2O_2 for 5 min.

Using this immunohistochemical approach, we observed nuclear AT8 staining in most brain regions. This pattern is unusual, as phospho-tau pathology in experimental models and human tauopathies is typically cytoplasmic and/or neuritic rather than nuclear. Nonetheless, similar nuclear staining has occasionally been detected in mouse brain tissue in related experimental approaches performed by our group [35–39,42,46]. To determine whether this signal reflected specific labeling or non-specific background, we performed additional controls. Omission of the primary antibody completely abolished the signal, confirming antibody dependence. Moreover, tissue from untreated animal models did not show any AT8-positive deposits, although the nuclear staining persisted (Supplementary Fig. 1 (A-D)). In parallel, immunohistochemistry using the AT8 primary antibody was performed on human AD brain sections, which showed the expected pattern of pathological tau immunoreactivity and a lack of tau or nuclear staining when the primary antibody was omitted (Supplementary Fig. 1 (E and F)). Together, these observations indicate that the apparent nuclear AT8 signal does not represent genuine tau pathology but rather non-specific background nuclear staining in mouse tissue. Accordingly, our interpretation focuses on cytoplasmic and process-associated AT8-positive deposits, which are not confounded by this background signal.

2.5. *Immunofluorescence in the hippocampus of inoculated Nfe2l2$^{-/-}$ and WT animals*

Double-labeling immunofluorescence was carried out on de-waxed sections, 4 μm thick. The sections were boiled in citrate buffer (pH = 6.0) or Tris-EDTA buffer (pH = 9.0) to enhance antigenicity and blocked for 30 min at room temperature with 10% fetal bovine serum diluted in 0.1 M phosphate-buffered saline (PBS). The sections were stained with a saturated solution of Sudan black B (Merck, DE) for 15 min to block autofluorescence of putative lipofuscin granules present in cell bodies, and then rinsed in 70% ethanol and washed in distilled water. Then, the sections were incubated at 4 °C overnight with combinations of AT8 and one of the following primary antibodies: GFAP (Rb, 1/400, RP014-S, Diagnostic BioSystems, Pleasanton, CA, USA), IBA1 (Rb, 1/1000, 019–19741, FUJIFILM Wako Chemicals, Osaka, Japan), NeuN (Rb, 1/200, ab177487, Abcam, Cambridge, UK), PLP1 (Rb, 1/100, SAB2101830, Merck, St. Louis, MO, USA) and OLIG2 (Rb, 1/500, AB9610, Millipore, Burlington, MA, USA). After washing, the sections were incubated with Alexa488 or Alexa546 fluorescence secondary antibodies against the corresponding host species. Nuclei were stained with DAPI. Then the sections were mounted in Immuno-FluoreTM mounting medium (MP Biomedicals, CA, United States), sealed, and dried overnight. Sections were examined with a Carl Zeiss LSM880 confocal microscope.

2.6. *Quantification of abnormal deposits revealed by IHC in the hippocampus of Nfe2l2$^{-/-}$ and WT animals*

Photomicrographs of hippocampal sections stained with the AT8 antibody were obtained at × 40 magnification, covering an area of 0.126 mm^2, using a DP25 camera mounted on an Olympus BX50 light microscope. For each slide, thirteen images of the hippocampal region were captured, including the CA subfields, dentate gyrus, and hilum, as well as adjacent areas where spreading has been reported here and previously [35–39,42], such as the corpus callosum (CC), corpus callosum radiation and the fimbria; with analyses performed across six z-levels per case next to the inoculation site. It is important to note that our previous publications have consistently reported that tau spreading remains largely restricted to areas near the injection site, although in some cases it extends to other regions after long post-injection incubation periods. However, at 3 months post-inoculation, animals poorly or did not show aggregates in distant brain regions [35–39,42]. In our case, no aggregates were observed in cortex, ventricular system, thalamus or ventral regions. Given this established pattern of localized propagation, our analysis focused on the hippocampus and adjacent regions where tau accumulation is most likely to occur under these experimental conditions.

Images were analyzed using Photoshop software. Both AD-inoculated and control-inoculated mice were assessed; control-inoculated mice did not show tau deposits. The density of tau staining was calculated as the intensity of the diaminobenzidine (DAB) precipitate pigment normalized for the total area and expressed as a percentage of arbitrary units per area. *Nfe2l2*$^{-/-}$ animals inoculated with vehicle or with PHFs extracted from control cases did not show any AT8-positive deposits in their brains, nor did WT animals under the same conditions, as we already demonstrated in the past [35,38,39,42], whereas animals inoculated with AD extracts did (Supplementary Fig. 2). Investigators taking photomicrographs were blinded to the identification of the mice. Because AT8-positive deposits frequently appeared as irregular aggregates within cellular processes, often forming perinuclear, cap-like, or comma-shaped structures rather than discrete, well-circumscribed inclusions, the boundaries of individual AT8-positive cells could not be reliably identified. In many cases, AT8 immunoreactivity extended along axons or oligodendroglial processes, producing continuous staining patterns that were not attributable to a single cell body. This morphology made it difficult, and in some regions impossible, to determine whether the staining belonged to one cell, multiple cells, or diffuse extracellular material. For these reasons, quantification based on cell counts would have introduced substantial bias and reduced reproducibility. Instead, measuring the area or intensity of AT8 staining provided a more accurate and biologically meaningful assessment of tau pathology. This approach captures the overall burden and distribution of phospho-tau deposits, independent of cell boundaries, and is therefore better suited to the type of AT8 staining observed in this study.

2.7. *Hippocampal RNA extraction*

For animal model multiomic molecular characterization, RNA was extracted from the hippocampal samples, using six animals, each 3 months old, from both WT and *Nfe2l2*$^{-/-}$ groups. The extraction was performed using the RNeasy Lipid Tissue Mini Kit (Qiagen, Hilden, Germany), following the manufacturer's instructions and protocol. The quality of the isolated RNA was initially assessed using the Bioanalyzer Assay (Agilent, Santa Clara, CA, USA). The concentration of each sample was determined by A260 measurements with the Nanodrop 1000 (Thermo Scientific, Wilmington, DE, USA). RNA integrity was evaluated using the Agilent 2100 BioAnalyzer (Agilent Technologies, Palo Alto, CA, USA).

2.8. *Transcriptomic analysis in the hippocampus of Nfe2l2$^{-/-}$ and WT animals*

2.8.1. *Transcriptomic analysis using RNA-seq*

The transcriptomic analysis was performed using RNA-seq technology. RNA libraries were first prepared using the NEBNext® Ultra II RNA Library Prep Kit (New England Biolabs), following the manufacturer's protocol. To validate the RNA samples, the RNA High Sensitivity TapeStation (Agilent Technologies) was used. For library preparation, 700 ng of RNA was utilized and validated using a DNA 1000 TapeStation Kit. Libraries were combined in equimolar ratios, and the resulting pool was quantified using qPCR before sequencing on two NextSeq High Output 2 × 75 runs (Illumina). Quality of raw paired-end sequencing reads was assessed using FastQC (version 0.11.7) [47] and MultiQC (version 1.21) [48]. Reads were aligned to the *Mus musculus* reference genome (GRCm39) using the STAR aligner (version 2.7.8a) [49] with the GENCODE vM34 basic gene annotation, using default parameters. The resulting SAM files were converted to BAM format, sorted by coordinate, and indexed using SAMtools (version 1.19.2) [50]. Duplicate reads were identified and removed using the MarkDuplicates function from Picard Tools (version 2.25.1) [51], and processed alignment files for the same sample were merged. Finally, gene-level expression was quantified by summarizing reads mapping to exonic regions using featureCounts from the Subread package (version 2.0.3) [52], and the results were aggregated into a single gene-by-sample count matrix for subsequent analysis. Differential expression analysis was performed in R (version 4.3.1) using the DESeq2 package (version 1.40.2) [53] on the aggregated gene count matrix. The analysis used a design formula of ~condition, and differentially expressed genes (DEGs) between knockout (*Nfe2l2*$^{-/-}$) and WT samples were identified using the Wald test. P-values were adjusted for multiple testing using the Benjamini-Hochberg (BH) method, and genes were considered significant with an adjusted p-value (padj) < 0.05 and an absolute log2 fold-change >0.58. Gene annotation, including the conversion of Ensembl IDs to gene symbols and the retrieval of gene biotypes, was performed using the biomaRt package (version 2.58.2) [54]. Results were visualized using heatmaps of scaled, normalized counts generated with the ComplexHeatmap package (version 2.16.0) [55]. Functional analysis of DEGs was performed using ShinyGO (v0.82) software [56]. ShinyGO's ranking system for gene enrichment analysis prioritizes results based on statistical significance (p-value and FDR) and the magnitude of enrichment (fold enrichment). Here, the 'Select by FDR, sort by fold enrichment' method was applied, which first filters gene sets based on FDR significance and then ranks the filtered results by fold enrichment. Transcriptomic research results files are included in Supplementary File 1.

2.8.2. Cell population association

To associate the RNA-seq expression profiles with hippocampal cell populations, we used the CellGO pipeline [57]. CellGO integrates transcriptomic signatures with single-cell reference datasets by combining gene ontology (GO)-based functional annotation and semantic similarity scoring. The adult mouse hippocampal single-cell RNA-seq reference dataset from Saunders et al. [58] was used as the cell-type reference. This dataset provides population-level transcriptional profiles for major hippocampal neuronal (excitatory and inhibitory), glial (astrocytes, oligodendrocytes, microglia), and vascular-associated (endothelial, pericyte) classes. From our RNA-seq data, DEGs were used as input query signatures for CellGO. GO enrichment analysis was performed on the query signatures, and the resulting functional profiles were compared with those of the reference populations. Semantic similarity scores between query and reference GO profiles were computed, and each query was assigned to the hippocampal cell type with the highest similarity. Statistical significance of cell-type associations was evaluated by permutation testing with 1000 randomizations, and only assignments with $p < 0.05$ were retained.

2.8.3. Weighted gene coexpression network analysis

WGCNA was done in R using the WGCNA library [59]. We first constructed a gene coexpression network based on pair-wise correlation of gene expression using all samples at the same time. Therefore, all subsequent analysis based on the coexpression network constructed with all samples used a soft-power threshold of 5. We identified modules of genes based on their topological overlap dissimilarity with their connection strengths in the weighted network [60,61]. Using the dynamic tree-pruning algorithm, 49 modules were obtained with highly correlated eigengenes (Pearson correlation >/ = 0.8); and genes not assigned to any module were labeled in gray. Module eigengenes were correlated to genotype. The *p*-values were obtained from a general univariate lineal model. GO enrichment analysis was performed using GOstats [62]. DEG with uncorrected *p*-values <0.01 for each contrast were used for functional analysis. All genes belonging to a particular gene coexpression module were also used for independent functional analyses. *P*-values for categories were adjusted considering FDR using Benjamini–Hochberg correction with the p. adjust function in R.

2.9. Gene expression validation using RT-qPCR

For transcriptomic validations, the retrotranscriptase reaction was carried out using a High-Capacity cDNA Archive Kit (Applied Biosystems, Foster City, CA, USA) following the protocol provided by the supplier. Duplicate TaqMan RT-qPCR assays were performed for each gene on previously obtained cDNA samples in 384-well optical plates using QuantStudio 7 Pro Real-Time PCR (Applied Biosystems, Foster City, CA, USA). In each well we added 2.25 μL of cDNA sample, and 2.75 μL of the master mix prepared with the probe. The master mix was TaqMan Universal PCR Master Mix (Applied Biosystems), and the TaqMan probe used was diluted 1:10 in it. We used the internal housekeeping genes, alanyl-tRNA synthase (*Aars*), glucuronidase B (*Gusβ*), hypoxanthine phosphoribosyltransferase 1 (*Hprt1*), and X-prolyl aminopeptidase (aminopeptidase P) 1 (*Xpnpep1*) for normalization. The reactions were carried out using the following parameters: 50 °C for 2 min, 95 °C for 10 min, and 40 cycles of 95 °C for 15 s and 60 °C for 1 min. Finally, all TaqMan PCR data were captured using the Data & Analysis 2 (DA2) Software (ThermoFisher). The identification numbers and names of all TaqMan probes used are shown in Table 1. The selection of these probes was based on RNA-seq results. Samples were analyzed with the double-delta cycle threshold (ΔΔCT) method.

2.10. Quantitative phosphoproteomics in the hippocampus of *Nfe2l2*$^{-/-}$ and WT animals

2.10.1. Sample preparation

For animal model molecular characterization, frozen hippocampal samples from 3-month-old *Nfe2l2*$^{-/-}$ and WT animals, with six animals per group were homogenized in a lysis buffer (8 M urea, 50 mM dithiothreitol (DTT), supplemented with protease (Complete Mini, Roche #11836153001) and phosphatase inhibitors (PhosSTOP, Roche #4906845001). Lysates were centrifuged at 20,000 g (1 h, 15 °C), and the resulting supernatant was quantified with the Bradford assay kit (BioRad, Barcelona, Spain). To obtain the phosphorylated peptide sample fraction, 600 μg of protein was separated for protein digestion. Proteins were reduced with DTT (final concentration of 20 mM; room temperature, 30 min), alkylated with iodoacetamide (final concentration of 30 mM; room temperature, 30 min in the dark), diluted to 0.9 M with ABC and digested with trypsin (Promega, Madison, WI, USA; 1:20 w/w enzyme protein ratio, 18 h, 37 °C). Protein digestion was interrupted by acidification (pH < 6, acetic acid), and the resulting peptides were cleaned-up using Pierce™ Peptide Desalting Spin Columns (ThermoFisher Sci., Waltham MA, USA). The following phosphorylated peptide enrichment was performed using the High-Select™ TiO2 Phosphopeptide enrichment Kit (ThermoFisher Sci., Waltham, MA, USA) according to the manufacturer's instructions. Finally, the enriched phosphopeptide sample fraction was cleaned-up as described before and dried down in a Speed-Vac system. A 10 μg aliquot of cleaned-up peptides from protein digestion was set aside for total protein analyses.

2.10.2. Data independent acquisition (DIA)-mass spectrometry

Dried down peptide samples were reconstituted with 2% ACN-0.1%

Table 1
List of TaqMan probes used to assess transcript levels by RT-qPCR.

Gene Name	Gene Symbol	Reference
Acetyl-CoA carboxylase alpha	*Acaca*	Mm01304257_m1
Alanyl-tRNA synthetase	*Aars*	Mm00507627_m1
Aldehyde dehydrogenase 1 family member L1	*Aldh1l1*	Mm03048957_m1
Allograft inflammatory factor 1	*Aif1*	Mm00479862_g1
Aquaporin 4	*Aqp4*	Mm00802131_m1
Apolipoprotein E	*Apoe*	Mm01307193_g1
Autophagy related 5	*Atg5*	Mm01187303_m1
Basic transcription factor 3-like 4	*Btf3l4*	Mm00659372_m1
Calcium Binding And Coiled-Coil Domain 2 (Nuclear Dot Protein 52)	*Npd52*	Mm01606381_gH
Catalase	*Cat*	Mm00437992_m1
Cathepsin C	*Ctsc*	Mm00515580_m1
Cathepsin G	*Ctsg*	Mm00456011_m1
Cathepsin S	*Ctss*	Mm01255859_m1
CD68 molecule	*Cd68*	Mm03047343_m1
CD74 molecule, major histocompatibility complex, class II	*Cd74*	Mm00658576_m1
C-X-C motif chemokine ligand 10	*Cxcl10*	Mm00445235_m1
GABA type A receptor associated protein like 1	*Atg8*	Mm00457880_m1
Glial fibrillary acidic protein	*Gfap*	Mm01253033_m1
Glucuronidase beta	*Gusb*	Mm01197698_m1
Glutathione S-transferase mu 1	*Gstm1*	Mm00833915_g1
Glutathione S-transferase mu 3	*Gtsm3*	Mm00833923_m1
Glutathione-disulfide reductase	*Gsr*	Mm00439154_m1
Heme oxygenase 1	*Hmox1*	Mm00516005_m1
Hypoxanthine phosphoribosyltransferase 1	*Hprt-1*	Mm01545399_m1
Inositol polyphosphate-5-phosphatase D	*Inpp5d*	Mm00494987_m1
Interferon beta 1	*Ifnb1*	Mm00439552_s1
Interferon gamma	*Ifng*	Mm01168134_m1
Interleukin 1 beta	*Il1b*	Mm00434228_m1
Interleukin 10	*Il10*	Mm00439614_m1
Interleukin 10 receptor subunit alpha	*Il10ra*	Mm00434151_m1
Interleukin 10 receptor subunit beta	*Il10rb*	Mm00434157_m1
Interleukin 6	*Il6*	Mm00446190_m1
Interleukin 6 signal transducer	*Il6st*	Mm00439665_m1
Kelch-like ECH-associated protein 1	*Keap1*	Mm00497268_m1
LDL Receptor Related Protein 1	*Lrp1*	Mm00464608_m1
MLX Interacting Protein Like	*Mlxipl*	Mm02342723_m1
Monoglyceride lipase	*Mgll*	Mm00449274_m1
NAD(P)H quinone dehydrogenase 1	*Nqo1*	Mm01253561_m1
Neuroblastoma suppressor of tumorigenicity 1	*Nbl1*	Mm00500746_m1
Nitric oxide synthase 1	*Nos1*	Mm00435175_m1
Nitric oxide synthase 2	*Nos2*	Mm00440502_m1
Nuclear factor, erythroid 2 like 1	*Nfe2l1*	Mm01299481_m1
Nuclear factor, erythroid 2 like 2	*Nfe2l2*	Mm00477784_m1
Prostaglandin-endoperoxide synthase 2	*Ptgs2*	Mm00478374_m1
S100 calcium-binding protein B	*S100b*	Mm00485897_m1
Sequestosome 1	*Sqstm1*	Mm00448091_m1
Solute carrier family 1 member 1 (Excitatory amino acid transporter 3)	*Slc1a1*	Mm00436590_m1
Solute carrier family 1 member 2 (Excitatory amino acid transporter 2)	*Slc1a2*	Mm01275814_m1
Solute carrier family 16 member 1 (Monocarboxylate transporter 1)	*Slc16a1*	Mm01306379_m1
Solute carrier family 16 member 3 (Monocarboxylate transporter 4)	*Slc16a3*	Mm01246825_m1
Solute carrier family 16 member 7 (Monocarboxylate transporter 2)	*Slc16a7*	Mm00441442_m1
Solute carrier family 2 member 1 (Glucose transporter type 1)	*Slc2a1*	Mm00441473_m1
Solute carrier family 2 member 3 (Glucose transporter type 3)	*Slc2a3*	Mm00441483_m1
Sulfiredoxin 1	*Srxn1*	Mm00769566_m1
Superoxide dismutase 2	*Sod2*	Mm01313000_m1
Synaptosome-associated protein 25	*Snap25*	Mm01276449_m1
Synaptotagmin 1	*Syt1*	Mm00436858_m1
Synaptotagmin 6	*Syt6*	Mm01308768_m1
Thioredoxin 2	*Txn2*	Mm00444931_m1
TNF receptor superfamily member 1 A	*Tnrsf1a*	Mm01182929_m1
Toll-like receptor 4	*Tlr4*	Mm00445273_m1
Toll-like receptor 7	*Tlr7*	Mm00446590_m1
Transforming growth factor beta 1	*Tgfb1*	Mm03024053_m1
Transforming growth factor beta 2	*Tgfb2*	Mm00436955_m1
Triggering receptor expressed on myeloid cells 2	*Trem2*	Mm04209424_g1
Tumor necrosis factor alpha	*Tnfa*	Mm99999068_m1
Unc-51 like autophagy activating kinase 1	*Ulk1*	Mm00437238_m1
Uncoupling protein 1	*Ucp1*	Mm01244861_m1
Vacuolar protein sorting 41	*Vps41*	Mm00548976_m1
X-prolyl aminopeptidase 1	*Xpnpep1*	Mm00460040_m1

FA (Acetonitrile-Formic acid), spiked with internal retention time peptide standards (iRT, Biognosys), and quantified by NanoDropTM spectrophotometer (ThermoFisher Sci.) prior to LC-MS/MS analysis using an EVOSEP ONE system coupled to an Exploris 480 mass spectrometer (Thermo Fisher Sci.). Peptides were resolved using C18 Performance column (75 μm × 15 cm, 1.9 μm particles; Evosep) with a predefined Xcalibur Whisper100 20 SPD (58min, IonOpticks Aurora Elite, EV1112) method. Peptides were ionized using 1.6 kV spray voltage at a capillary temperature of 275 °C. Sample data were acquired in data-independent acquisition (DIA) mode with full MS scans (scan range: 400–900 *m/z*; resolution: 60,000; maximum injection time: 22 ms; normalized AGC target: 300%) and 24 periodical MS/MS segments applying 20 Th isolation windows (0.5 Th overlap: Resolution: 15000; maximum injection time: 22 ms; normalized AGC target: 100%). Peptides were fragmented using a normalized HCD collision energy of 30%.

2.10.3. Bioinformatics and statistical analysis

Mass spectrometry data files were analyzed using Spectronaut (Biognosys) by direct DIA analysis (dDIA). MS/MS spectra were searched against the Uniprot proteome reference from mouse database using standard settings. Enzyme was set to trypsin in a specific mode. On the one hand, Carbamidomethyl (C) was set as a fixed modification, and oxidation (M), acetyl (protein N-term), deamidation (N), and Gln-> pyro-Glu as variable modifications for total protein analysis. On the other hand, Carbamidomethyl (C) was set as a fixed modification, and oxidation (M), acetyl (protein N-term), and Phospho (STY) as variable modifications for phospho-proteome analysis. Identifications were filtered by a 1% Q-value.

The obtained quantitative data for total protein were exported to Perseus software (version 1.6.15.0) [63] for statistical analysis and data visualization. For total protein analysis, unpaired Student's *t*-test was used for direct comparisons. Statistical significance was set at p-value lower than 0.05 in all cases and 1% peptide FDR threshold was considered. Differentially expressed proteins were considered significant when their absolute fold change was below 0.77 (downregulated proteins) and above 1.3 (up-regulated proteins) in linear scale. Quantitative data obtained from the phosphoproteome were collapsed using a custom coded plugin Peptide Collapse (v.1.4.4) in Perseus (v.1.6.15.0) that convert a normal Spectronaut report into a site-level report [64]. Plugin settings were set as default grouping posttranslational modifications (PTMs) by sample (FileName), collapsing matrix by site-level and setting the PTM localization probabilities filter at more than 0.75. Statistical analyses were conducted following the same protocol as the total protein study. MS data and search results files were deposited in the Proteome Xchange Consortium via the JPOST partner repository (https://repository.jpostdb.org) [65] with the identifier PXD067832 for ProteomeXchange and JPST004047 for jPOST (for reviewers: https://repository.jpostdb.org/preview/46744637668b04ab6d8d48; Access key: 5267).

Proteomic experiments generate a large number of peptides or proteins that need to be independently evaluated using statistical tests and may yield type I errors [66]. However, it is well recognized that the statistical power of proteomic datasets is often limited by sample size, technical variability, and the intrinsic complexity of peptide quantification. Under these conditions, the application of stringent multiple testing corrections, such as FDR adjustment, may dramatically reduce sensitivity and fail to identify even biologically meaningful changes [67]. In the present study, the group size and the magnitude of observed fold changes were therefore considered critical determinants for interpreting the data. For this reason, uncorrected p-values combined with fold-change thresholds were used to define differentially expressed proteins, allowing the detection of potentially relevant candidates that might otherwise be excluded by conservative corrections. Functional analysis of clusters of deregulated proteins was then performed using ShinyGO (v0.82) software [56], as described above, to assess whether these candidates converged on biologically coherent pathways, thereby reducing the likelihood of spurious findings.

2.11. *Electrophoresis and immunoblotting in the hippocampus of Nfe2l2$^{-/-}$ and WT animals*

For confirmation of the proteomic analyses, we used frozen hippocampal samples from 3-month-old *Nfe2l2*$^{-/-}$ and WT animals, with six animals per group, that were homogenized in RIPA lysis buffer (50 mM Tris-HCl buffer pH 8, 2,5 M NaCl, 20% SDS, 5% Na-deoxycholate) supplemented with protease and phosphatase inhibitors (Roche, Basel, Switzerland). After adding the buffer, samples were left in the cold chamber for 1 h spinning. Then, they were centrifuged for 20 min at 20,000 rpm at 4 °C. Protein concentration was determined with the bicinchoninic acid (BCA) method (Thermo Scientific, MA, USA). Equal amounts of protein (13 μg) for each sample were loaded and separated by electrophoresis on 12% sodium dodecyl sulfate polyacrylamide gel electrophoresis (SDS-PAGE) gels and transferred onto nitrocellulose membranes (Amersham, Freiburg, Germany). To avoid nonspecific bindings, membranes were incubated in 5% nonfatty milk in Tris-Buffered Saline (TBS) containing 0,2% Tween (TBS-T) for 40 min. After washing, membranes were incubated with the primary antibody (Table 2) overnight at 4 °C. Next day, membranes were incubated for 1 h with the appropriated HRP-conjugated secondary antibody (1:2000, Dako, Glostrup, Denmark). Protein loading was controlled using β-actin (42 kDa, 1:40.000, Sigma, MO, USA). In cases where molecular weights of protein of interest and β-actin overlapped, total protein was used instead. Membranes were revealed using a chemiluminescence reagent (ECL, Amersham). Densiometric quantification was performed with the ImageLab v4.5.2 software (BioRad).

2.12. *Statistics*

Normality of the distributions was studied using D'Agostino & Pearson test. If values followed a normal distribution, unpaired Student's t-test was used to compare two groups, in case that not followed normal distribution, Mann Whitney test was used to compare two groups. Graphic representations were done using GraphPad Prism version 9.5 (La Jolla, CA, USA). Data is expressed as mean ± SEM. Significance levels between *Nfe2l2*$^{-/-}$ and WT mice were set at $* p < 0.05$, $**p < 0.01$, and $***p < 0.001$.

Table 2
List of antibodies used to assess protein levels by western blotting.

Antibody	Supplier	Reference	Host	Dilution
4-HNE	Abcam	ab46545	Rb	1/1000
8-OHdG	Abcam	ab26842	Ms	1/1000
ALDH1L1	Abcam	ab56777	Ms	1/1000
AQP4	Abcam	ab9512	Ms	1/1000
GFAP-C-terminal	Abcam	ab48050	Rb	1/1000
GFAP	DAKO	Z0334	Rb	1/400
GSR	Abcam	ab16801	Rb	1/2000
MDAL	Academy BioM	MD20a-R1a	Rb	1/1000
p-GFAP	Abcam	ab115898	Ms	1/1000
GSTM2	Abcam	ab208639	Rb	1/500
YKL40	Invitrogen	PA5-43746	Rb	1/500
GSK3-α/β	Stressgen	KAM-ST002C	Ms	1/1000
GSK3β-*p*-Ser9	Cell Signaling	9336	Rb	1/1000
p38 MAPK	Cell Signaling	9211	Rb	1/1000
TAU-5	Abcam	ab80579	Ms	1/500
3R-tau	Upstate	05–803	Ms	1/1000
4R-tau	Abcam	ab242333	Rb	1/500
p-Tau (Ser422)	Invitrogen	44-764G	Rb	1/1000
VIM	Abcam	ab92547	Rb	1/1000
β-actin	Abcam	ab49900	HRP	1/25000
β-actin	Sigma Aldrich	A5316	Ms	1/40000

3. Results

To begin characterizing the impact of NRF2 deficiency on brain function and tau pathology, we first assessed the general phenotype and baseline cognitive performance of *Nfe2l2*$^{-/-}$ mice at 3 months of age. Using the novel object recognition test, no significant differences were observed in the discrimination index between WT (RI: 0.33) and *Nfe2l2*$^{-/-}$ (RI: 0.32) mice [t(23) = 0.20, p = 0.84]. In addition, no macroscopic differences in brain morphology were detected by histological analysis with hematoxylin and eosin staining, GFAP and IBA1. Following this initial characterization, we then investigated how NRF2 deficiency modulates tau seeding and spreading mechanisms *in vivo* after hippocampal inoculation with human AD-derived paired helical filaments (PHFs).

3.1. *NRF2 deficiency impairs tau seeding and spreading in the hippocampus*

To study the impact of the molecular alterations reported in the *Nfe2l2*$^{-/-}$ model on tau protein seeding and spreading mechanisms, 3-month-old mice were inoculated with human p-tau (PHFs) derived from AD V-VI brain, according to previous reports [35–39]. In addition, PHFs extraction solution (vehicle) and brain PHFs extract from brain case with no neuropathological aggregates were inoculated as controls. Western blot confirmation of tau content was performed using an anti-p-Tau-Ser422 antibody to assess the full banding pattern of the PHF-insoluble fraction. In AD case at Braak stages V–VI, this analysis revealed three prominent bands at approximately 68, 64, and 60 kDa, together with oligomeric smears. Unspecific band is observed at 45 kDa. In contrast, control cases did not show positive tau banding patterns (Fig. 1).

Inoculation of exogenous human tau was performed in both *Nfe2l2*$^{-/-}$ and WT mice. The actuation framework, although robust and comparable to previously applied experimental designs in the field, is also restricted by the appearance of pathological features in this model, which typically emerge later in life. Brain tissue alterations, such as vacuolar leukoencephalopathy, develop between eight and twelve months of age [23], with preservation observed up to six months of age [28]. In addition, we did observe substantial reproductive challenges in the *Nfe2l2*$^{-/-}$ colony, including reduced fertility and smaller litter sizes, which posed limitations for colony expansion and experimental throughput.

For these reasons, after 3 months, the brains were extracted to study p-tau protein spread. In WT the immediate vicinity of the hippocampus puncture and along the corpus callosum reported tau aggregates, with a greater amount of exogenous tau in the WT mice compared to the *Nfe2l2*$^{-/-}$ mice (Fig. 1). In this last model, spreading of tau aggregates beyond the puncture site was surprisingly not observed in *Nfe2l2*$^{-/-}$ animals, just showing few aggregates or none around the inoculation site. Specifically, tau-immunoreactive cells, revealed with the AT8 antibody, were observed in ipsilateral neurons of the dentate gyrus region of the hippocampus, and also in cells (mainly coiled bodies) located in the hilus in both animal models (Fig. 1A–D). AT8 antibody immunoreactivity was also observed in glial cells of the fimbria and corpus callosum. These cells were often located at the border between the alveus of the hippocampus and the corpus callosum, forming row-like aggregates, similar to what we previously observed in other studies (Fig. 1E–H). *Nfe2l2*$^{-/-}$ mice showed few immunoreactive glial cells and

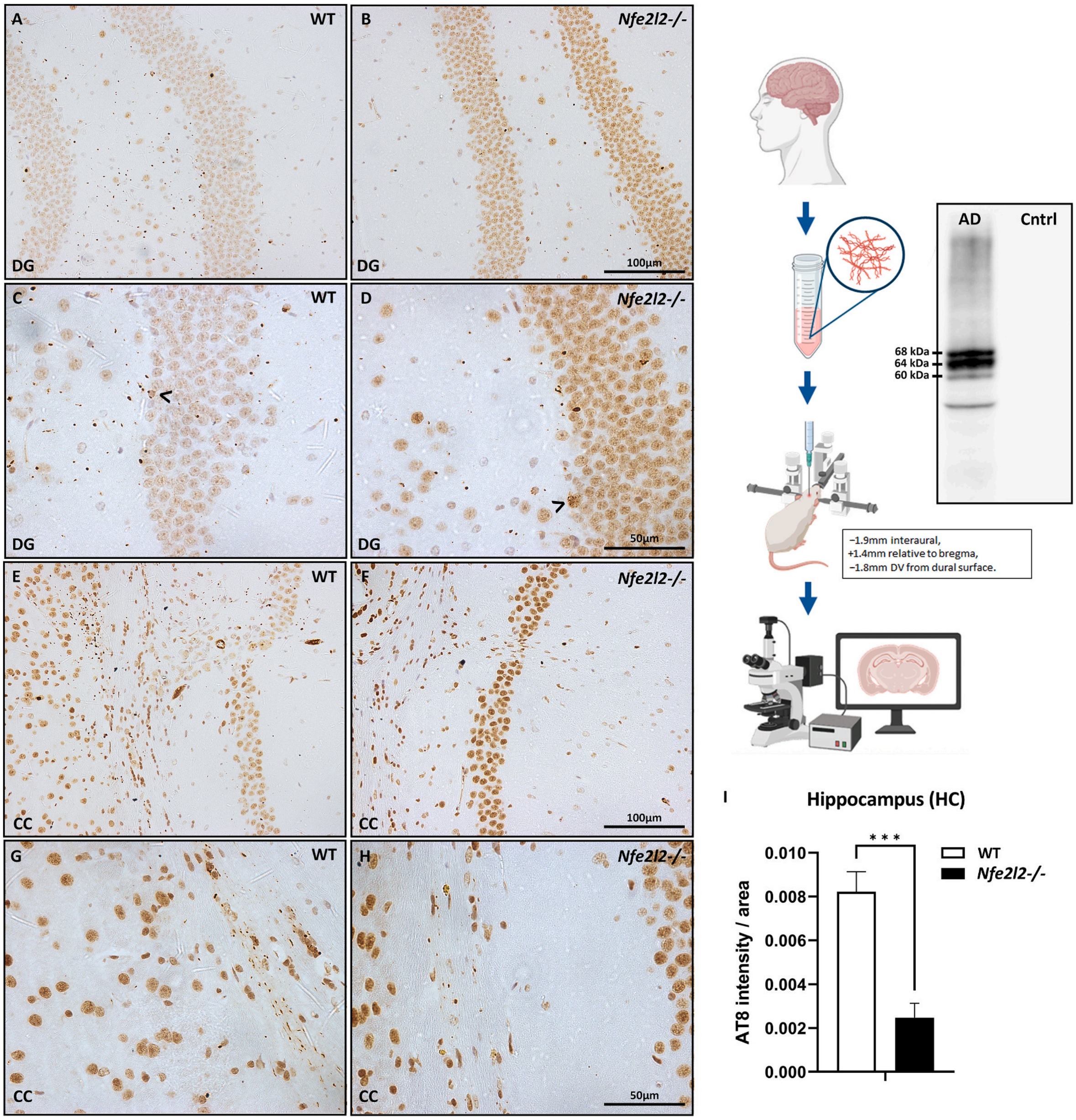

Fig. 1. Hyperphosphorylated tau-containing cells and threads following unilateral intrahippocampal injection of human p-tau into WT and *Nfe2l2*$^{-/-}$ mice aged 3 months old and sacrificed at 6 months of age. Characterization of the sarkosyl-insoluble AD fraction inoculated into both animal models is shown in the experimental scheme by Western blotting of the phospho–Tau (Ser422) band pattern (scheme). The total p-Tau seeding and spreading across the dentate gyrus (DG) and hilum of the hippocampus (**A-D**) and in the corpus callosum (CC) and corpus callosum radiation (CCR) is higher in WT mice inoculated with AD homogenates than in AD-inoculated *Nfe2l2*$^{-/-}$ mice (**E-H**). AT8 antibody decorates the nuclei of some neurons (arrows) and glial cells in form of coiled coils or "comas" in *Nfe2l2*$^{-/-}$ and WT mice (**C-D**). Semiquantification, performed using a minimum of six slides/Z-levels per animal in hippocampal regions and adjacent areas where spreading is reported (CC, CCR, fimbria), demonstrated a significant reduction in the number of AT8-positive cytoplasmic deposits, as well as AT8-immunoreactive threads and dots, in the *Nfe2l2*$^{-/-}$ mice ($n = 11$) compared with WT mice ($n = 7$) (**I**). Significance was set at ***$p < 0.001$. Scale = 100 μm for A, B, E and F, and scale = 50 μm for C, D, G and H.

threads and limited to the ipsilateral and middle regions of the corpus callosum, whereas most WT animals showed more abundance staining, arriving to the contralateral corpus callosum. All these findings were confirmed through semi-quantification, which verified that p-tau protein aggregates were significantly fewer in *Nfe2l2*$^{-/-}$ mice compared with WT animals. An unpaired two-tailed Student's *t*-test revealed a marked reduction in the measured parameter in *Nfe2l2*$^{-/-}$ mice relative to WT controls ($t = 5.169$, $p = 0.0001$). The effect size, expressed as $\eta^2 = 0.6404$, indicated a large effect (Fig. 1I).

3.2. Cell-type–specific localization of phospho-Tau in brains of mouse models inoculated with PHFs derived from human AD brains

Double-label immunofluorescence was used to identify the cellular substrates of tau seeding and propagation in both animal models by assessing AT8-positive phospho-tau deposits. Using markers for neurons (NeuN), axonal projections (PLP1), microglia (IBA1), astrocytes (GFAP), and oligodendroglial lineages (OLIG2), we determined the cellular identity of tau-accumulating cells. We found that AT8-positive labeling was mainly restricted to regions adjacent to the puncture site, particularly within the corpus callosum. We focused on this localization because it is consistent with the more limited tau seeding and spreading observed in the *Nfe2l2*$^{-/-}$ model and allows direct comparison of cellular populations between the two models in the same region.

Following inoculation with AD sarkosyl-insoluble fractions, no phospho-tau deposits were detected in astrocytes (GFAP) in either model within the corpus callosum (Fig. 2a–h). Likewise, phospho-tau accumulation in microglia (IBA1) was not observed in this region (Fig. 2i–p). In the corpus callosum, aggregates were not detected in neurons (NeuN) in either model; however, a small number of adjacent CA1 neurons in WT animals exhibited AT8 immunoreactivity (white arrows) (Fig. 2q–x). The vast majority of AT8-positive structures in the corpus callosum were identified as axonal projections or oligodendrocytes in both models, as indicated by PLP1 (Fig. 3a–h) and OLIG2 labeling (Fig. 3i–p), respectively. In this region, phospho-tau deposits were predominantly perinuclear in oligodendrocytes or distributed along cellular processes, frequently forming cap-like or comma-shaped structures reminiscent of coiled bodies observed in human tauopathies (white arrows in magnified images; Fig. 3q–t).

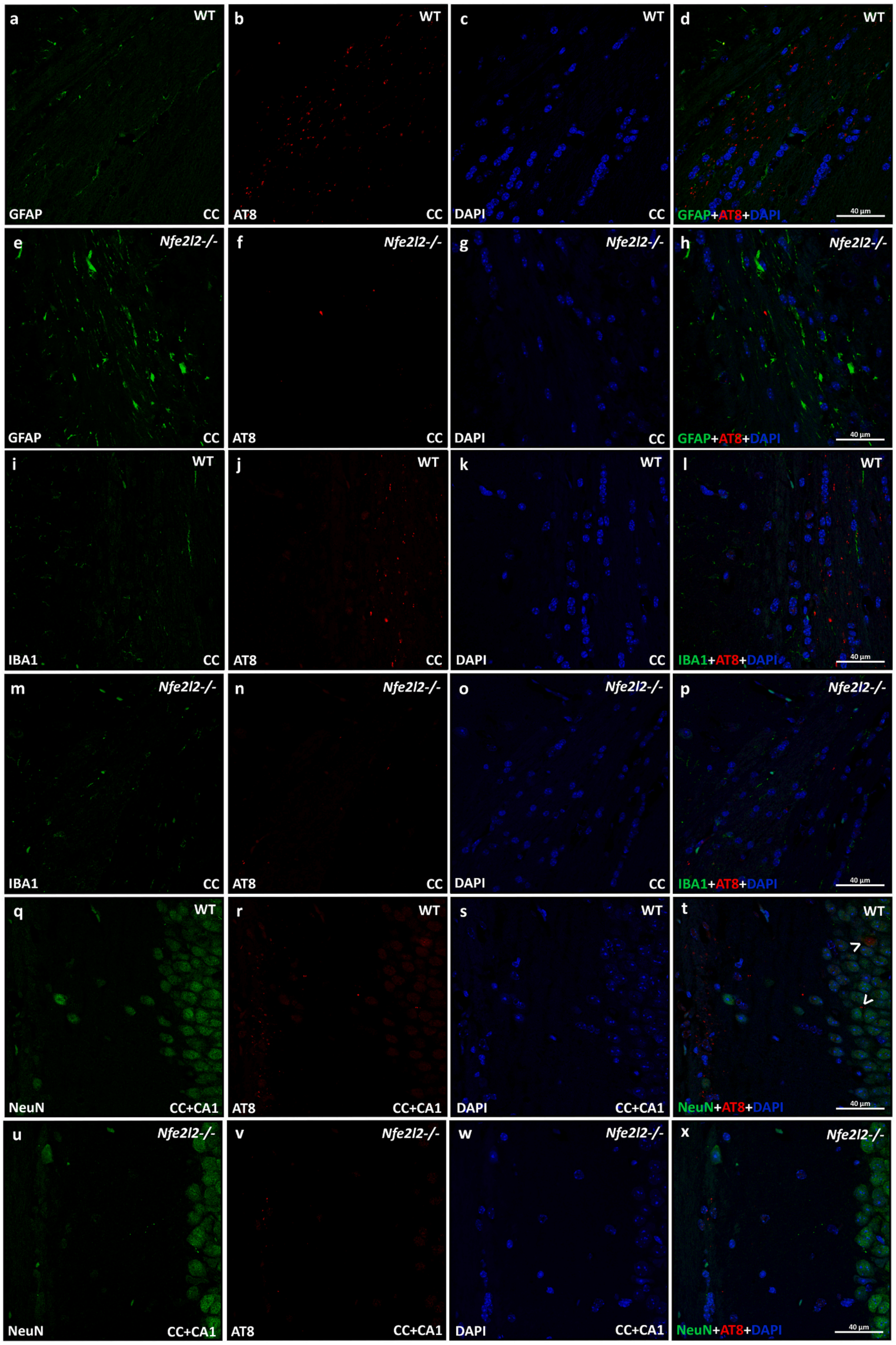

Fig. 2. Phospho-tau localization in WT and *Nfe2l2*$^{-/-}$ mice after AD inoculation is not located in neurons, microglia or astrocytes in the corpus callosum. Double-label immunofluorescence and confocal microscopy for cell-type markers (GFAP, IBA1, NeuN) (green) and AT8 (red) in WT and *Nfe2l2*$^{-/-}$ mice inoculated with sarkosyl-insoluble AD fractions into the hippocampus at 3 months of age and analyzed at 6 months (3-month survival). Tau deposits were observed along the corpus callosum (CC) in both genotypes, with no phospho-tau detected in astrocytes (GFAP) **(a–h)**, microglia (IBA1) **(i–p)** or neurons (NeuN) **(q–x)**. However, some nuclei or perineuronal spaces in the CA1 region of WT animals showed positivity, consistent with areas where tau pathology had spread (indicated with white arrows) **(q–x)**. Nuclei were stained with DAPI (blue). Scale bar = 40 µm.

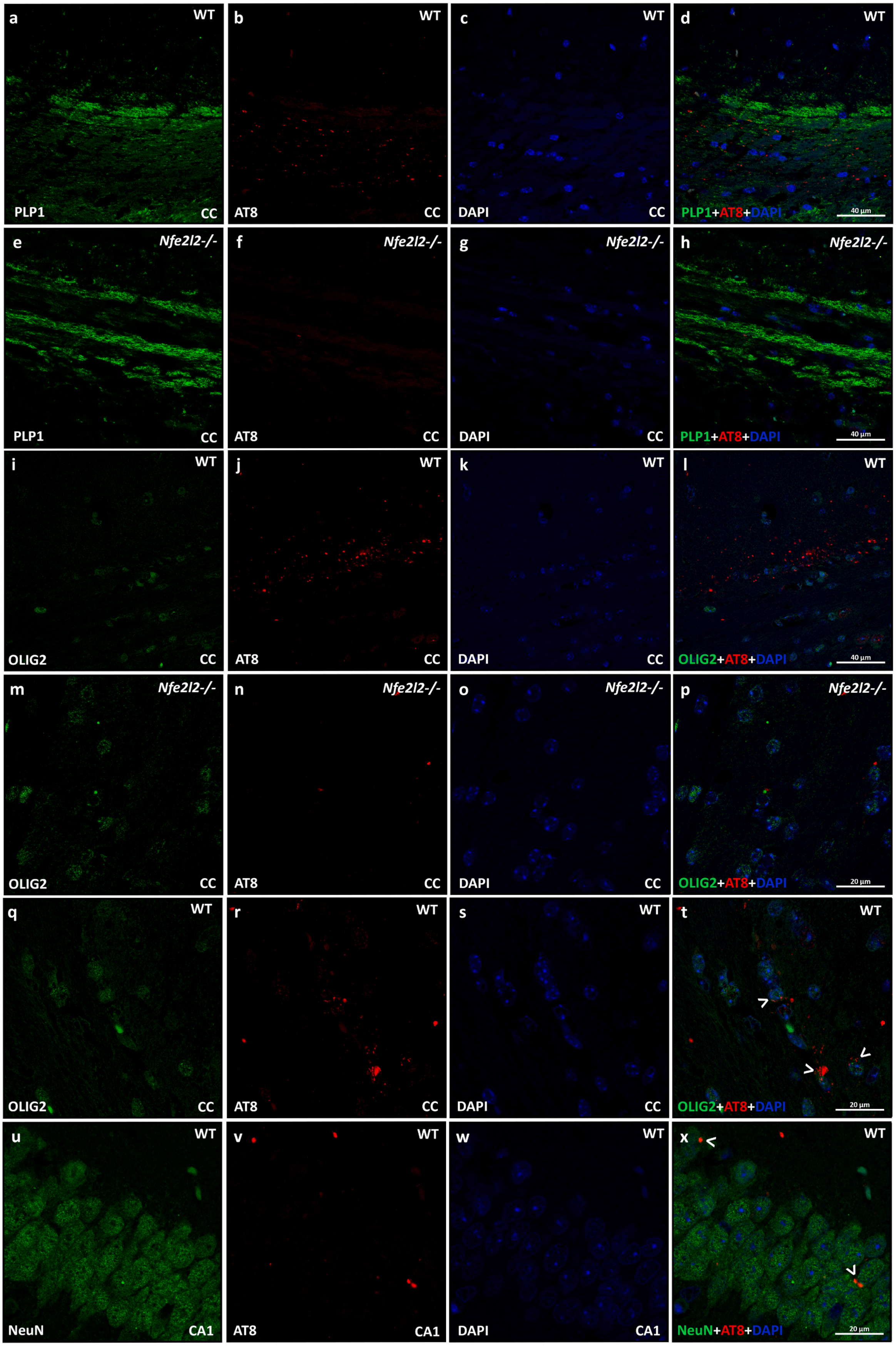

(caption on next page)

Fig. 3. Phospho-tau localization in WT and *Nfe2l2*$^{-/-}$ mice after AD inoculation is restricted to oligodendrocyte and fibers in the corpus callosum and neurons in the hippocampus. Double-label immunofluorescence and confocal microscopy for axonal projections and oligodendrocyte markers (PLP1 and OLIG2) (green) and AT8 (red) in WT and *Nfe2l2*$^{-/-}$ mice inoculated with sarkosyl-insoluble AD fractions into the hippocampus at 3 months of age and analyzed at 6 months (3-month survival). Tau deposits were observed along the corpus callosum (CC) in both genotypes, with phospho-tau detected in nervous fibers **(a–h)** and oligodendrocytes **(i–t)**. In the CC, phospho-tau deposits were predominantly perinuclear in oligodendrocytes or distributed along cellular processes, frequently forming cap-like or comma-shaped structures reminiscent of coiled bodies observed in human tauopathies (indicated with white arrows). In the hippocampus, aggregates were also present (AT8, red), mainly in WT animals and not in *Nfe2l2*$^{-/-}$ due its less seeding and spreading capacity, being located in neurons (NeuN, green) in the CA1 (indicated with white arrows) **(u–x)**. Nuclei were stained with DAPI (blue). Scale bar = 40 or 20 μm.

In contrast, in WT animals, phospho-tau deposits were present and widely distributed throughout the hippocampus in the CA regions, where they were detected in neurons and their projections. These deposits were observed both in perinuclear regions and along cellular processes, frequently forming cap-like or comma-shaped structures, as indicated by white arrows in the magnified images (Fig. 3u-x).

3.3. Molecular characterization of the Nfe2l2$^{-/-}$ *hippocampus*

After establishing that 3 months *Nfe2l2*$^{-/-}$ mice display impaired tau seeding and spreading following hippocampal inoculation, we next sought to characterize the underlying molecular alterations associated with this protective NRF2 deficiency. To this end, we performed an

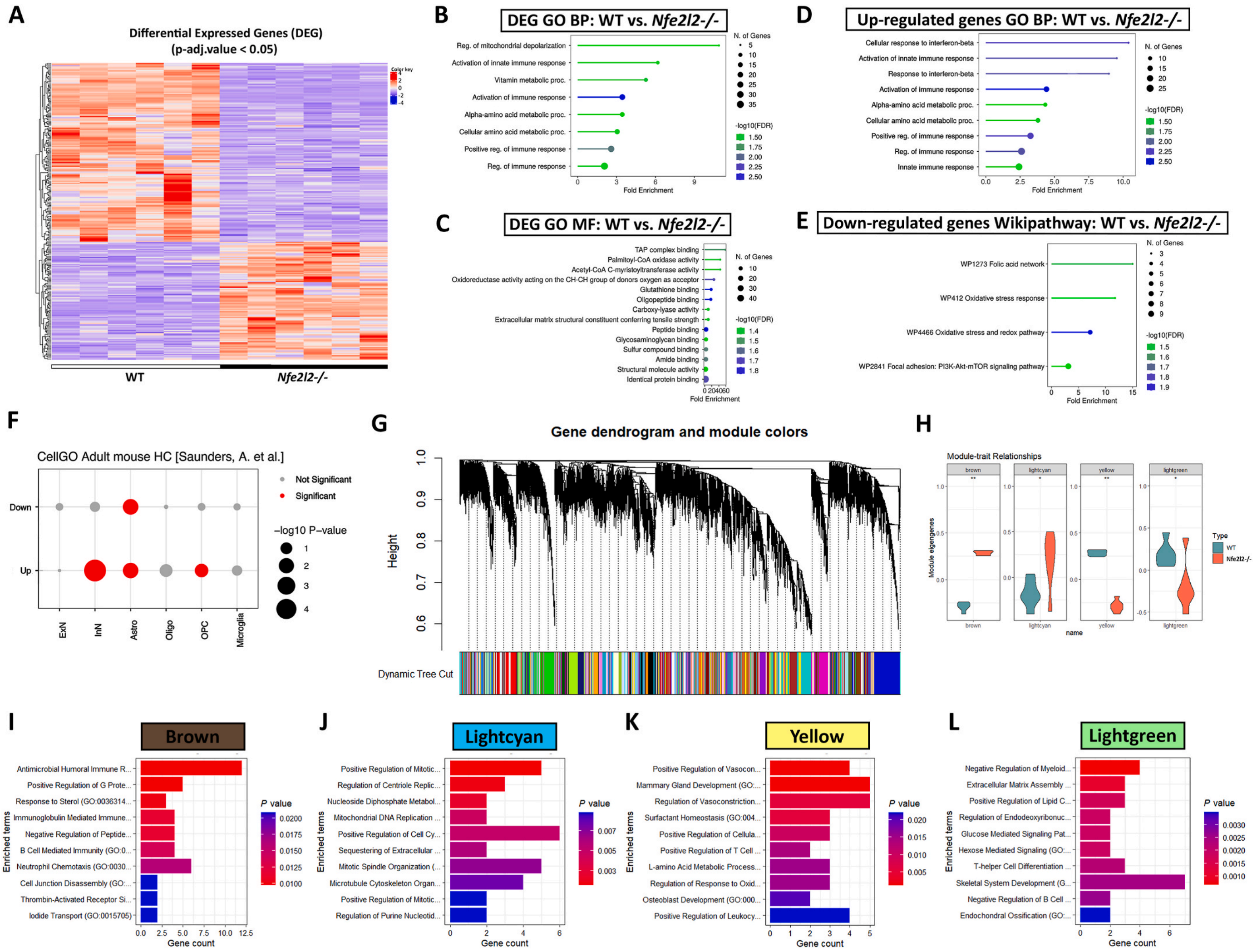

Fig. 4. Transcriptomic profiling, functional enrichment, and network analysis of hippocampal gene expression in *Nfe2l2*$^{-/-}$ and WT mice. (A) Heat map representing deregulated transcripts at a probability of an adjusted p-value <0.05. White boxes correspond to WT mice, and black boxes correspond to *Nfe2l2*$^{-/-}$ mice; **(B–C)** Functional analysis of all DEG against the GO biological processes (BP) and Molecular Function (MF) databases ($p < 0.05$). **(D)** Functional analysis of all significant up-regulated genes against the Gene Ontology biological processes (BP) database ($p < 0.05$). **(E)** Functional analysis of all significant down-regulated genes against the Wikipathways database ($p < 0.05$). For all functional graphs **(B–E)**, the blue-green color spectrum beneath each gene category is proportional to the enrichment FDR score number obtained from the differentially expressed proteins involved in the functional group. Dot size reflects the number of altered genes belonging to the category. **(F)** DEG clusterization according to cell types signatures of adult mouse hippocampus (HC) dataset (Saunders et al.). **(G)** Weighted GENE coexpression network analysis (WGCNA) of transcriptome identifies 48 gene modules. Modules are labeled by color and number (M1 to M48). Proteins not assigned to any particular coexpression modules were labeled M0 or gray. Dendrogram obtained by hierarchical clustering of proteins based on their topological overlap is shown at the top. **(H)** Modul-trait relationships between groups. Mann–Whitney-Wilcoxon test analysis revealed distinct significant changes in module eigengene expression among groups in 4 different modules. **(I–L)** Identification of gene enriched GO terms in each significant module was performed for modules characterization.

integrative, multi-omics approach combining RNA-seq, WGCNA, quantitative RT-qPCR validation, proteomics, phosphoproteomics, and targeted Western blot analyses. This comprehensive strategy enabled us to capture transcriptional, proteomic, and post-translational changes, thereby providing a systems-level view of how NRF2 loss impacts. The following sections detail these analyses and highlight convergent mechanisms through which NRF2 regulates hippocampal homeostasis and vulnerability to tau pathology.

3.3.1. RNA-seq analysis of *Nfe2l2*$^{-/-}$ hippocampus highlights immune activation and cell-type-specific changes

To investigate differential gene expression in the *Nfe2l2*$^{-/-}$ hippocampus compared to WT animals, we performed transcriptomic analyses using RNA-seq. To account for sex differences, we included three males and three females per genotype, all at three months of age. No significant sex-related effects were observed, and transcriptomic changes were primarily associated with genotype differences. After data filtering, we identified 2860 transcripts that were significantly altered (p-value <0.05), with 745 transcripts remaining significant after adjustment (adjusted p-value <0.05). Among these deregulated transcripts, 327 were downregulated and 418 were upregulated. Focusing specifically on protein-coding genes, 202 were downregulated and 263 were upregulated in the hippocampus of *Nfe2l2*$^{-/-}$ mice. A heatmap illustrates the expression patterns of these deregulated transcripts (Fig. 4A). A table with the list of up-regulated and down-regulated genes is provided in Supplementary Material S1.

Functional enrichment analysis using the Gene Ontology (GO) database revealed several biological process clusters associated with the differentially expressed genes ($p < 0.05$). The most prominent altered biological processes were related to the immune response, including terms such as “regulation of mitochondrial depolarization”, “activation of innate immune response”, “vitamin metabolic process”, “activation of immune response”, “alpha-amino acid metabolic process”, “cellular amino acid metabolic process”, “positive regulation of immune response”, and “regulation of immune response” (Fig. 4B). Further functional analysis based on molecular function indicated that the deregulated genes were primarily involved in oxidoreductase metabolism and protein binding activities. These clusters included terms such as “TAP complex binding”, “palmitoyl-CoA oxidase activity”, “acetyl-CoA C-myristoyltransferase activity”, “oxidoreductase activity acting on the CH–CH group of donors with oxygen as acceptor”, “glutathione binding”, “oligopeptide binding”, “carboxy-lyase activity”, “extracellular matrix structural constituent conferring tensile strength”, “peptide binding”, “glycosaminoglycan binding”, “sulfur compound binding”, “amide binding”, “identical protein binding”, and “structural molecule activity” (Fig. 4C).

When examining the functional enrichment of DEGs based on the direction of regulation, we found that upregulated genes were enriched in GO biological process clusters associated with immune response and amino acid metabolism. These included “cellular response to interferon-beta”, “activation of innate immune response”, “response to interferon beta”, “activation of immune response”, “alpha-amino acid metabolic process”, “cellular amino acid metabolic process”, “positive regulation of immune response”, “regulation of immune response”, and “innate immune response” (Fig. 4D). Although several genes were downregulated, GO analysis did not yield significant clusters for this group. However, WikiPathways analysis revealed that downregulated genes were significantly associated with pathways such as “folic acid network”, “oxidative stress response”, “oxidative stress and redox pathway”, and the “focal adhesion: PI3K-Akt-mTOR signaling pathway” (Fig. 4E).

Given the importance of cellular specialization in the mammalian brain, we also performed cell-type enrichment analysis using the CellGO adult mouse hippocampus database [58]. This analysis revealed that loss of NRF2 significantly alters the transcriptomic profiles of specific hippocampal cell populations, with upregulation of genes associated with inhibitory neurons, astrocytes, and oligodendrocyte progenitor cells (OPCs), and downregulation of genes linked to astrocytic populations (Fig. 4F).

Globally, loss of NRF2 elicits a reprogramming of the hippocampal transcriptome marked by coordinated activation of innate/IFN-β–responsive immune modules and remodeling of amino-acid/vitamin metabolic pathways, accompanied by functional shifts toward oxidoreductase and diverse binding activities. In parallel, pathways linked to folate/redox homeostasis and focal-adhesion PI3K–Akt–mTOR signaling are selectively attenuated. Cell-type–level enrichment further indicates engagement of inhibitory neuronal, astroglial, and OPC gene programs with subset-specific astrocytic downregulation. Collectively, these data position NRF2 as a key regulator of hippocampal immune–metabolic balance and cell-type programs, providing a framework for subsequent mechanistic interrogation.

3.3.2. Coexpression network analysis identifies genotype-linked gene modules enriched in immune, cell cycle, and developmental pathways

Beyond differential expression, WGCNA provided additional insight by revealing coordinated gene modules, hub genes, and pathway-level regulation that are not detectable with standard RNA-seq analysis alone. WGCNA was constructed using the expression values of all genes with variable expression among the 12 samples. 48 uncorrelated ($r < 0.8$ gene modules were identified and labeled by colors and numbers (M1 to M48). The genes not assigned to any particular coexpression module were assigned to M0 or “gray” (Fig. 4G). We obtained the most representative pattern of gene expression across all samples for each one of these modules by calculating the eigengene (i.e., the first principal component). The eigengene of each module was then correlated with the genotype obtaining an eigengene significance for each module using Mann–Whitney-Wilcoxon test. Two modules, M12-brown (515 genes) and M13-lightcyan (411 genes), were positively correlated with *Nfe2l2*$^{-/-}$ genotype. Two modules, M26-yellow (103 genes) and M28-lightgreen (97 genes), were negatively correlated with *Nfe2l2*$^{-/-}$ genotype (Fig. 4H). For modules characterization, identification of gene enriched GO terms in each significant module was performed.

The M12-Brown module is characterized by significant enrichment in immune-related GO terms. The top enriched pathway is “Antimicrobial Humoral Immune Response,” followed closely by “Positive Regulation of G Protein-Coupled Receptor Signaling Pathway.” Additional enriched processes include “Response to Sterol,” “Immunoglobulin Mediated Immune Response,” and “Negative Regulation of Peptidase Activity.” Notably, immune cell-related pathways such as “B Cell Mediated Immunity” and “Neutrophil Chemotaxis” also appear, indicating a strong association with both innate and adaptive immune responses. The P values for these terms range from 0.01 to 0.02, with gene counts primarily between 2 and 12, suggesting moderate to strong enrichment significance (Fig. 4I).

In the M13-Lightcyan module, the enriched terms are predominantly linked to cell cycle regulation and DNA replication. The most significantly enriched GO term is “Positive Regulation of Mitotic Cell Cycle,” followed by “Regulation of Centriole Replication” and “Nucleoside Diphosphate Metabolic Process.” Other relevant pathways include “Mitochondrial DNA Replication” and “Microtubule Cytoskeleton Organization,” suggesting this module is involved in cellular proliferation and structural organization. The p-values for these terms fall in the range of 0.003–0.007, with gene counts from 2 to 6, underscoring the robustness of these associations (Fig. 4J).

The M26-Yellow module demonstrates enrichment in developmental and regulatory processes, particularly those involved in tissue and organogenesis. Key GO terms include “Positive Regulation of Vasoconstriction,” “Mammary Gland Development,” and “Regulation of Vasoconstriction.” Additional terms such as “Surfactant Homeostasis” and “Osteoblast Development” further highlight the module's relevance to structural and functional development in various tissues. The associated p-values span from 0.005 to 0.02, with gene counts ranging between 1 and 5, indicating selective but biologically meaningful enrichment (Fig. 4K).

The M28-Lightgreen module is significantly enriched in immune and skeletal development-related pathways. The most prominent GO term is “T-helper Cell Differentiation,” followed by “Hexose Mediated Signaling Pathway” and “Extracellular Matrix Assembly.” Additional enriched processes include “Regulation of Endocytobiosis,” “Negative Regulation of Myeloid Cell Differentiation,” and “Endochondral Ossification.” This combination of immune signaling and developmental terms suggests a dual functional role. P-values for these terms are highly significant, ranging from 0.001 to 0.03, and gene counts vary between 1 and 6, supporting the functional coherence of the module (Fig. 4L).

Together, these network-level analyses pinpoint four genotype-associated coexpression programs that stratify the *Nfe2l2*$^{-/-}$ hippocampus. Eigengene–genotype correlations (Mann–Whitney–Wilcoxon) highlight two positively associated modules—M12-brown (immune/inflammatory, stress and GPCR signaling) and M13-lightcyan (cell-cycle/DNA replication/mtDNA and cytoskeletal organization)—indicating coordinated activation of immune and proliferative circuitry in NRF2 deficiency. Conversely, two negatively associated modules—M26-yellow (developmental and regulatory processes, including vasoconstriction and tissue maturation) and M28-lightgreen (ECM/ossification with immune lineage differentiation cues)—suggest attenuation of morphogenetic and matrix-remodeling pathways. Collectively, the WGCNA framework complements the DEG-based results, revealing that loss of NRF2 reshapes hippocampal gene programs toward immune activation and cell-cycle engagement while dampening tissue-developmental and extracellular-matrix modules.

3.3.3. RT-qPCR confirms disruption of NRF2 signaling and highlights inflammatory and astrocytic transcript changes

Based on the DEG revealed by RNA-seq analysis and functional clusters determination, the confirmation of genes coding for different components of the altered pathways was validated using RT-qPCR. Initially, genes related to the NRF2-Keap1 pathway were assessed to validate the direct effect on this pathway due to the knockout of the *Nfe2l2* gene.

The analysis of gene-coding proteins involved in the NRF2 downstream components pathway revealed that *Nfe2l2* ($p = 0.00014$), *Keap1* ($p = 0.013$) and *Nqo1* ($p = 0.0013$) were significantly reduced in *Nfe2l2*$^{-/-}$ animals compared to the WT model using t-Student's test. In contrast, no significant changes were observed in *Hmox1* ($p = 0.68$) (Fig. 5A). Additionally, we assessed several downstream effectors associated with antioxidant and oxidative stress responses within the NRF2–Keap1 pathway. The expression of *Cat* ($p = 0.001$), *Gsr* ($p = 0.0001$), *Gstm1* ($p = 0.0033$), *Nos1* ($p = 0.027$), *Sod2* ($p = 0.0046$), and *Srxn1* ($p = 0.0075$) using Student's t-test, which were significantly downregulated in *Nfe2l2*$^{-/-}$ animals compared to WT animals. However, *Txn2* ($p = 0.15$) and *Nos2* ($p = 0.13$) did not show significant differences between groups (Fig. 5B). Moreover, genes related to regulators of gene expression and the cellular stress response, indirectly associated with the NRF2-Keap1 pathway, were evaluated using Student's t-test. Only *Nbl1* ($p = 0.000$) showed a significant reduction in *Nfe2l2*$^{-/-}$ mice compared to WT animals, whereas *Nfe2l1* ($p = 0.18$) and *Btf3l4* ($p = 0.6$) did not show significant differences. Additionally, *Gstm3* expression levels were too low to obtain results (Fig. 5B).

Alterations in the NRF2-Keap1 pathway can significantly impact

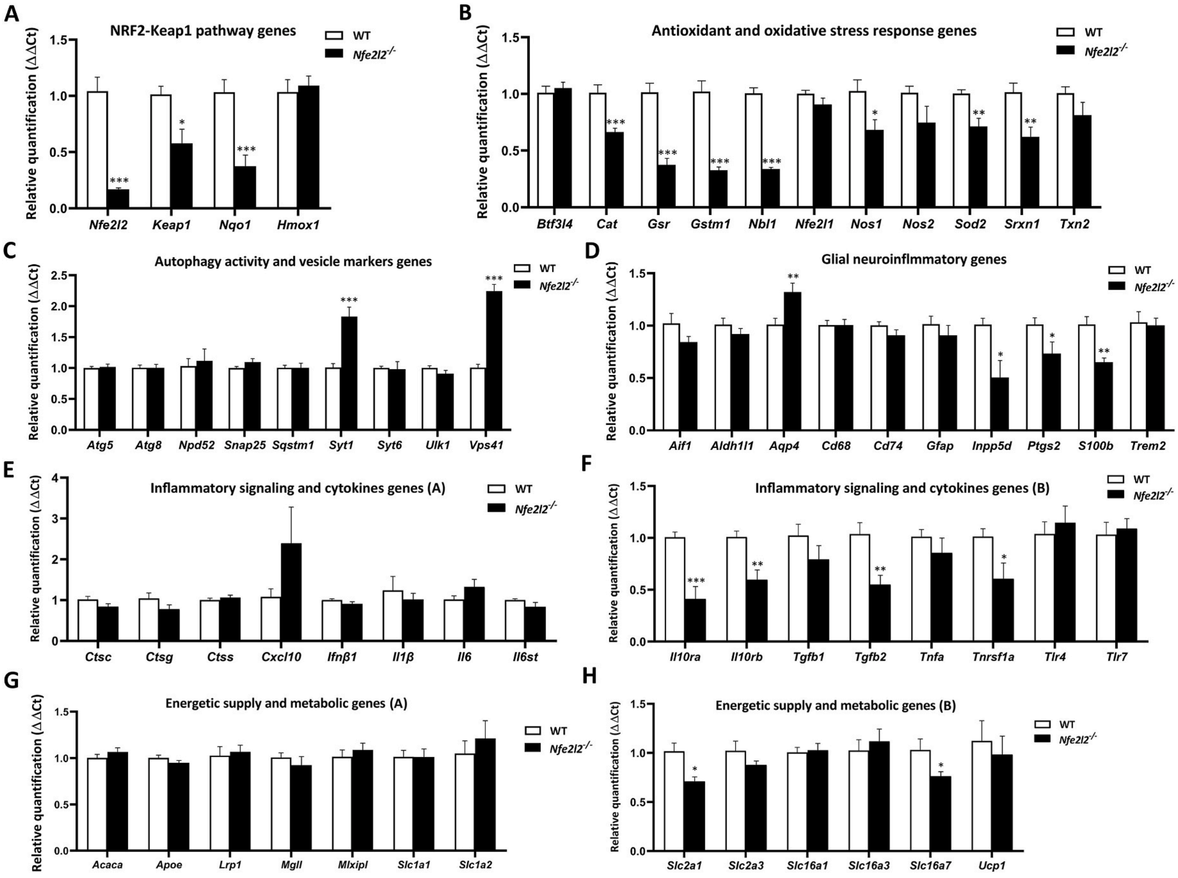

Fig. 5. qPCR validation of hippocampal transcripts associated with altered pathways in *Nfe2l2*$^{-/-}$ and WT mice. Selected transcripts, identified based on potentially altered pathways and RNA-seq results, were analyzed by qPCR in the hippocampus of 3-month-old *Nfe2l2*$^{-/-}$ ($n = 6$) and WT ($n = 6$) mice. Transcripts are grouped according to their associated pathways: (A) NRF2–Keap1 pathway-related genes; (B) antioxidant and oxidative stress response genes; (C) autophagy activity and vesicle marker genes; (D) glial neuroinflammatory genes; (E, F) inflammatory signaling and cytokine genes (sets A and B); (G, H) energetic supply and metabolic genes (sets A and B). Statistical significance between groups was defined as $^{*}p < 0.05$, $^{**}p < 0.01$, and $^{***}p < 0.001$.

autophagic activity, prompting us to validate the expression profile of its main components, as NRF2 regulates the expression of autophagy-related genes. Main components of autophagic mechanisms were evaluated, but not significant changes were reported in the expression levels of *Sqstm1* ($p = 0.99$), *Npd52* ($p = 0.71$), *Atg5* ($p = 0.71$), *Atg8* ($p = 0.99$) and *Ulk1* ($p = 0.16$), when compared *Nfe2l2*$^{-/-}$ and WT animals using Student's t-test. Other vesicular markers of autophagy and/or neurotransmission were evaluated, revealing significant up-regulated levels in *Nfe2l2*$^{-/-}$ animals when compared to WT animals in *Vps41* ($p = 0.000$) and *Syt1* ($p = 0.000$) genes using t-Student's test, but not in *Snap25* ($p = 0.14$) and *Syt6* ($p = 0.86$) expression levels (Fig. 5C).

Based on the immune response clusters, we also evaluated neuroinflammatory markers associated with microglia and astrocytes. Microglial markers with reported deregulation included *Inpp5d* ($p = 0.015$), which was significantly reduced in *Nfe2l2*$^{-/-}$ compared to WT using Student's t-test. However, *Aif1* ($p = 0.13$), *Trem2* ($p = 0.82$), *Cd68* ($p = 0.06$), and *Cd74* ($p = 0.18$) did not show significant differences between groups. As for astroglial markers, no changes were observed in *Gfap* ($p = 0.38$) and *Aldh1l1* ($p = 0.28$) using t-Student's test, whereas *S100b* ($p = 0.0014$) and *Ptgs2* ($p = 0.05$), and *Aqp4* ($p = 0.015$) showed a significant difference to be downregulated and upregulated in *Nfe2l2*$^{-/-}$ animals compared to WT, respectively (Fig. 5D).

Next, based on functional analysis, pathways related to components involved in inflammatory signaling and cytokines were assessed too. Among the different general inflammatory transcripts evaluated, only *Il10ra* ($p = 0.001$), *Il10rb* ($p = 0.0037$), *Tgfb2* ($p = 0.0065$) and *Tnrsf1a* ($p = 0.037$) showed significantly downregulated levels in *Nfe2l2*$^{-/-}$ animals when compared to WT animals using Student's t-test. In contrast, the remaining mediators evaluated - *Il1β* ($p = 0.57$), *Il6* ($p = 0.19$), *Il6st* ($p = 0.16$), *Tnfa* ($p = 0.34$), *Cxcl10* ($p = 0.17$), *Ctsc* ($p = 0.13$), *Ctsg* ($p = 0.16$), *Ctss* ($p = 0.46$), *Tgfb1* ($p = 0.20$), *Tlr4* ($p = 0.60$), *Tlr7* ($p = 0.72$) and *Ifnβ1* ($p = 0.51$) – did not show significant changes between groups using Student's t-test. mRNA levels of *Ifn γ* and *Il10* were also assessed, but their expression levels were too low to obtain results (Fig. 5E and F).

Finally, based on the whole image of gene deregulation and the fact that NRF2-Keap1 pathway plays a critical role in the metabolic support provided by astrocytes, particularly in maintaining redox balance, energy homeostasis, and glucose metabolism; we assessed the expression of different transcripts related to these pathways. We evaluated genes implied in lipid transport and metabolic supplying, discovering significant down expression in astrocytic transporters *Slc2a1* ($p = 0.01$) and *Slc16a7* ($p = 0.05$) when comparing *Nfe2l2*$^{-/-}$ animals to WT animals using t-Student's test. In contrast, no changes were present between groups in genes coding for lipid and other metabolite transporters, such as *Acaca* ($p = 0.31$), *Apoe* ($p = 0.20$), *Lrp1* ($p = 0.75$), *Mgll* ($p = 0.45$), *Mlxipl* ($p = 0.49$), *Slc1a1* ($p = 0.98$), *Slc1a2* ($p = 0.51$), *Slc2a3* ($p=0.212$), *Slc16a3* ($p = 0.59$), *Slc16a1* ($p = 0.81$), and *Ucp1* ($p = 0.63$) (Fig. 5G and H).

Globally, the orthogonal validation by RT-qPCR corroborates the RNA-seq findings and confirms a primary attenuation of the NRF2–Keap1 axis and its antioxidant effector program in the *Nfe2l2*$^{-/-}$ hippocampus (reduced *Nfe2l2*, *Keap1*, *Nqo1*, and multiple ROS-detoxifying enzymes, with *Hmox1* spared). Core autophagy transcripts were unchanged, while increases in vesicle/trafficking markers (*Vps41*, *Syt1*) suggest synaptic/vesicular remodeling rather than overt autophagy rewiring. Neuroinflammatory readouts point to a nuanced glial phenotype: microglial *Inpp5d* was reduced without broad activation markers, astrocytic *S100b* and *Ptgs2* decreased whereas *Aqp4* increased, and key anti-inflammatory/cytokine-signaling components (*Il10ra*, *Il10rb*, *Tgfb2*, *Tnfrsf1a*) were downregulated in the absence of a canonical cytokine surge. Finally, diminished astrocytic nutrient-support transcripts (*Slc2a1* and *Slc16a7*) indicate compromised glucose/lactate handling, with other lipid/metabolite transporters largely unchanged. Overall, these validations reinforce that NRF2 loss weakens hippocampal redox defenses and glial metabolic support while reshaping vesicular and immune-signaling tone, aligning with a state of altered—rather than overtly heightened—neuroinflammation.

3.3.4. Proteomic profiling confirms synaptic and immune-related alterations in the hippocampus of *Nfe2l2*$^{-/-}$ mice

The total number of proteins quantified by SWATH-MS across all hippocampus samples was 3880. Multivariate and univariate statistical analyses were conducted, revealing that there was a differentiation observed in hippocampus protein profiles between *Nfe2l2*$^{-/-}$ and control groups. We observed that principal component analysis (PCA) of the hippocampus proteome was able to clearly separate the two groups using three components, explaining 25.4% (PC1), 17.4% (PC2) and 14.8% (PC3) of the total variability (Fig. 6A). Among these 3880 identified proteins, only 157 proteins were found as differentially expressed proteins (DEP) after FDR correction and applying a cut-off p-value below 0.05, and with an absolute fold-change of less than 0.77 (down-regulation) or greater than 1.3 (up-regulation) in linear scale. A volcano plot was generated to visualize the differential phosphorylation between *Nfe2l2*$^{-/-}$ and WT hippocampus samples, highlighting significantly deregulated proteins based on both fold change and statistical significance, showing 67 downregulated and 90 upregulated proteins when comparing WT against *Nfe2l2*$^{-/-}$ animals (Fig. 6B). These data are included in the MS data and search results files were deposited in the Proteome Xchange Consortium via the JPOST partner repository.

A heat-map represents the intensity of changes in DEPs (Fig. 6C). In addition to coloring boxes based on protein intensities, the cluster heatmap reordered the columns of the matrix (samples) based on the results of hierarchical clustering of protein intensities. Dendrograms were displayed in the top margin, representing sample classification based on protein profile similarities, which also corresponded homogeneously to sample group.

The functional significance of differential proteomes when compared WT and *Nfe2l2*$^{-/-}$ was assessed by functional enrichment analysis against Gene Ontology terms associated to cellular components (CC) and biological processes (BP). When analyzing our dataset in relation to cellular component functional clusters, we observe the involvement of genes in the inflammatory complement complex, including the “complement component C1 complex” and “complement component C1q complex.” These also map to key synaptic structures such as the “postsynapse,” “synaptic membrane,” “presynapse,” “cell body,” “synapse,” “cell junction,” and “plasma membrane region,” alongside associations with mitochondrial proteins (Fig. 6D). In terms of biological process clusters, the most prominently altered proteins are linked to synaptic functions, encompassing categories like “regulation of neurotransmitter levels,” “cellular amino acid metabolic processes,” “*trans*-synaptic signaling,” “chemical synaptic transmission,” “anterograde *trans*-synaptic signaling,” and “synaptic signaling.” These also include metabolic pathways such as “carboxylic acid metabolic processes,” “oxoacid metabolic processes,” “organic acid metabolic processes,” and “small molecule metabolic processes” (Fig. 6E).

Moreover, when we conducted an in-depth study of DEP functionality based on the type of deregulation using GO terms associated with biological processes and cellular components, we did not find terms related to molecular function, we observed certain particularities. When we associate these downregulated proteins with GO cellular component terms, we find that they are linked to “glial cell projection,” “SNARE complex,” “synapse,” and “mitochondria” (Fig. 6F). For the downregulated proteins, GO terms associated with biological processes suggested a global enhancement of functional clusters linked to synaptic processes, including groups such as “cellular amino acid metabolic processes,” “chemical synaptic transmission,” “anterograde *trans*-synaptic signaling,” “*trans*-synaptic signaling,” and “synaptic signaling.” Additionally, they encompassed functional groups related to metabolic processes, such as “cellular amino acid metabolic processes,” “carboxylic acid metabolic processes,” “oxoacid metabolic processes,” “organic acid metabolic processes,” “small molecule metabolic processes,” and

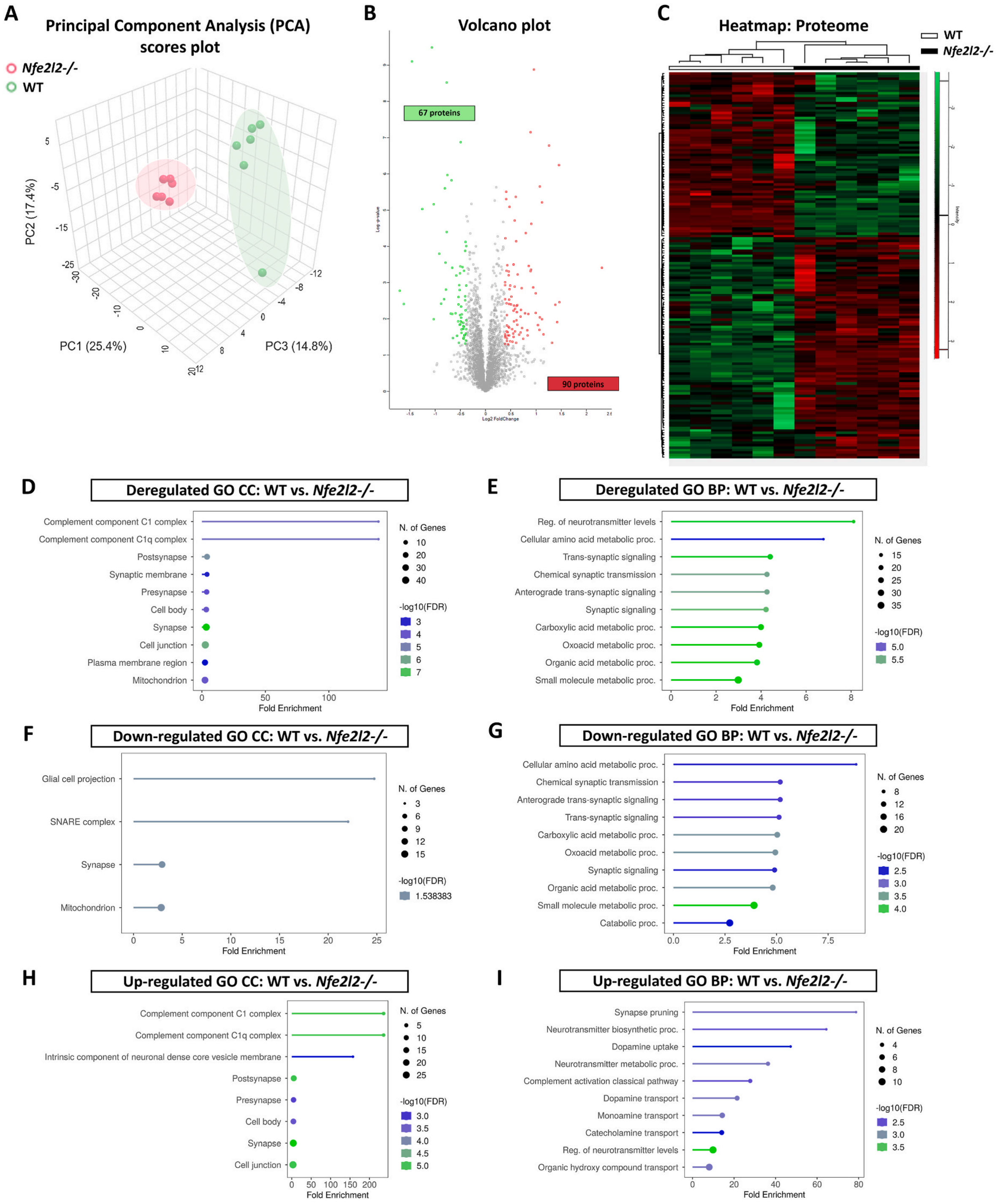

Fig. 6. Proteomic profiling and functional enrichment analysis of hippocampal proteins in *Nfe2l2*$^{-/-}$ and WT mice. (A) PCA using three principal components clearly separated the two groups (*Nfe2l2*$^{-/-}$ and WT). **(B)** Volcano plot showing 67 downregulated and 90 upregulated proteins when compare WT against *Nfe2l2*$^{-/-}$ animals. **(C)** Proteome heatmap of the hippocampus displaying 157 differentially expressed proteins. In both plots, red indicates upregulated expression and green indicates downregulated expression; color intensity reflects the magnitude of change. **(D–I)** Functional analysis of key deregulated proteins in the hippocampus of *Nfe2l2*$^{-/-}$ mice based on GO enrichment. The blue–green color scale beneath each category is proportional to the enrichment FDR score obtained from the differentially expressed proteins in that functional group. Dot size reflects the number of altered proteins within each category. **(D)** All deregulated proteins based on GO cellular components. **(E)** All deregulated proteins based on GO biological processes. **(F)** Downregulated and **(H)** upregulated proteins associated to GO cellular components terms. **(G)** Downregulated and **(I)** upregulated proteins related to GO biological processes terms.

“catabolic processes” (Fig. 6G).

In contrast, when up-regulated DEPs were associated with GO terms related to cellular components and biological processes, a strong association with synaptic structures and processes was observed. GO terms linked to cellular components terms suggested a global enhancement of proteins involved in the inflammatory complement complex, including the “complement component C1 complex” and “complement component C1q complex,” as well as synaptic structures such as the “postsynapse,” “presynapse,” “cell body,” “synapse,” “cell junction,” and “intrinsic component of neuronal dense core vesicle membrane” (Fig. 6H). In addition, when DEPs are associated to biological processes suggested a global enhancement of functional clusters, including "synapse pruning," "neurotransmitter biosynthetic processes," "dopamine uptake," "neurotransmitter metabolic processes," "complement activation, classical pathway," "dopamine transport," "monoamine transport," "catecholamine transport," "regulation of neurotransmitter levels," and "organic hydroxy compound transport" (Fig. 6I).

Globally, our data reveal a coherent, genotype-linked remodeling of the hippocampal proteome in *Nfe2l2*$^{-/-}$ mice, mapping on synaptic compartments and mitochondria, with a prominent enrichment of complement C1/C1q complexes. Upregulated proteins align with complement activation and synapse-remodeling programs (e.g., synapse pruning) and with neurotransmitter biosynthesis/transport, including monoamine pathways. In contrast, downregulated proteins map to glial projections, SNARE/vesicular machinery, mitochondria, and processes underpinning chemical/*trans*-synaptic signaling and amino/organic-acid metabolism. Thus, proteomic signatures indicate that loss of NRF2 directs the hippocampus toward complement-associated synaptic remodeling and neurotransmitter metabolic rewiring while attenuating elements of synaptic transmission and core metabolic support—mirroring the immune–metabolic shifts observed at the transcript level.

3.3.5. Quantitative phosphoproteomics identifies altered synaptic and cytoskeletal regulation in Nfe2l2$^{-/-}$ *hippocampus*

A total of 12,303 phosphosites were quantified by SWATH-MS across all hippocampus samples, corresponding to 2596 unique proteins. Both multivariate and univariate statistical analyses were conducted,

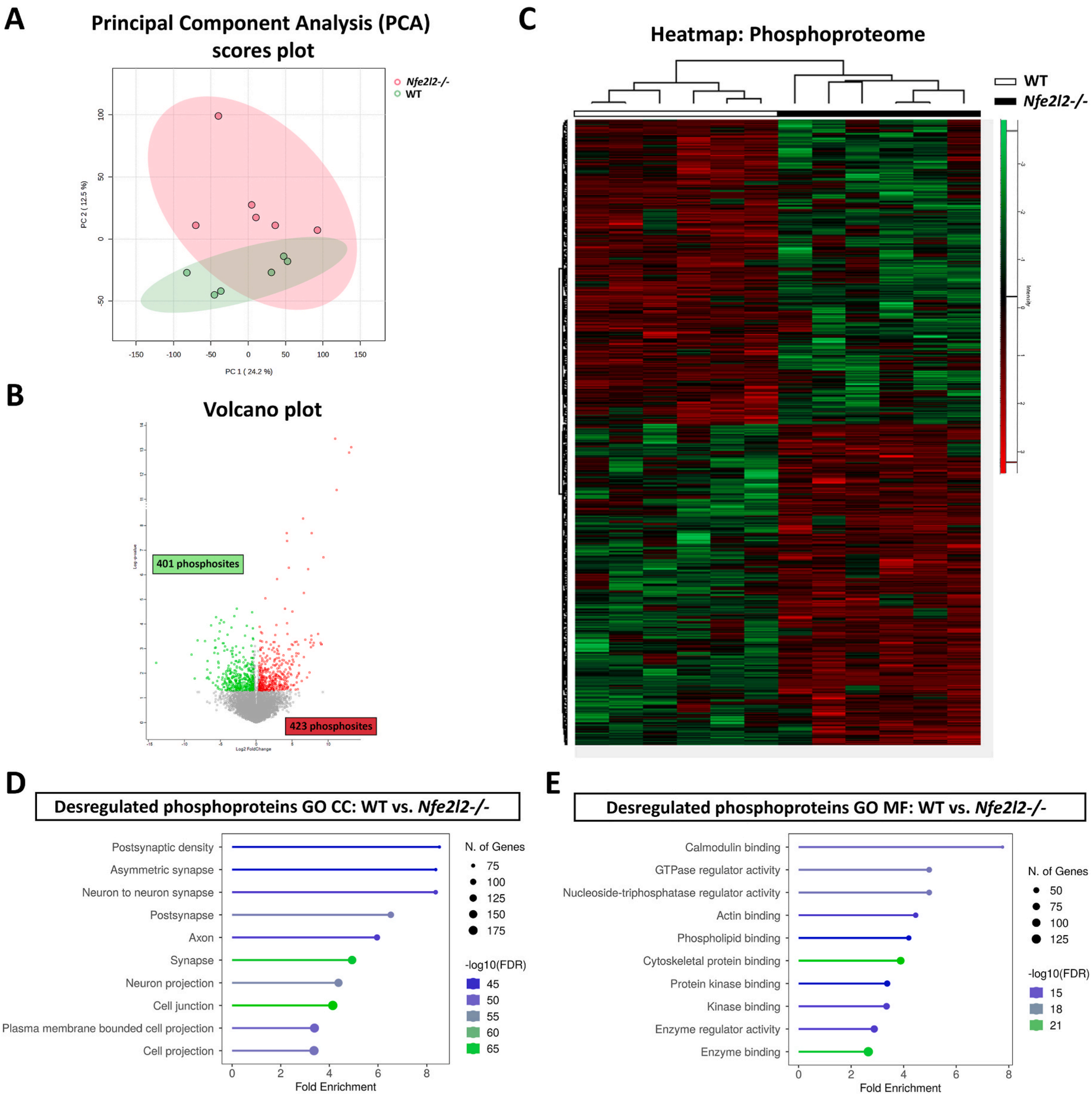

Fig. 7. Phosphoproteomic profiling and functional enrichment analysis of hippocampal phosphosites in *Nfe2l2*$^{-/-}$ and WT mice. (A) PCA using two principal components partially separated the two groups (*Nfe2l2*$^{-/-}$ and WT). **(B)** Volcano plot showing 401 downregulated and 423 upregulated phosphosites when comparing WT and *Nfe2l2*$^{-/-}$ animals. **(C)** Phosphoproteome heatmap of the hippocampus displaying 824 differentially expressed phosphosites. In both plots, red indicates upregulated expression and green indicates downregulated expression; color intensity reflects the magnitude of change. **(D, E)** Functional analysis of key deregulated proteins in the hippocampus of *Nfe2l2*$^{-/-}$ mice based on GO enrichment. The blue–green color scale beneath each category is proportional to the enrichment FDR score obtained from the differentially expressed proteins in that functional group. Dot size reflects the number of altered proteins within each category. **(D)** All deregulated proteins associated with altered phosphosites based on GO cellular components. **(E)** All deregulated proteins associated with altered phosphosites based on GO molecular function terms.

revealing distinct differences in hippocampal protein profiles between the *Nfe2l2*$^{-/-}$ and control groups. These analyses were used to assess global protein expression patterns and identify potential sample clustering trends. PCA was used to reduce data dimensionality and uncover the underlying structure in the dataset by capturing the major sources of variance across all samples. This analysis revealed a clear, though not complete, separation between WT and *Nfe2l2*$^{-/-}$ samples, with the first two principal components explaining 24.2% (PC1) and 12.5% (PC2) of the total variance, respectively (Fig. 7A).

Univariate analysis identified 370 dysregulated phosphorylated proteins, corresponding to 824 phosphosites. Among these, 401 phosphosites were significantly downregulated in *Nfe2l2*$^{-/-}$ animals, while 423 were significantly upregulated following the selection criteria exposed above for proteomic data. The direction of dysregulation (hyper- or hypophosphorylation compared to WT) varied depending on the specific protein and phosphorylation site, with no consistent pattern observed. Several phosphoproteins exhibited multiple phosphorylation sites, and the direction of phosphorylation was independent of the specific site affected. A volcano plot was created to visualize differential phosphorylation sites between *Nfe2l2*$^{-/-}$ and WT hippocampus samples, highlighting significantly dysregulated phosphosites based on both fold change and statistical significance (Fig. 7B). These data are included in the MS data and search results files were deposited in the Proteome Xchange Consortium via the JPOST partner repository.

A phosphoproteome heatmap revealed significant differences in protein phosphorylation levels in the hippocampus between WT and *Nfe2l2*$^{-/-}$ mice (Fig. 7C). Beyond visualizing protein intensities through color gradients, the clustered heatmap also rearranged sample columns according to hierarchical clustering results. Dendrograms shown above the heatmap depicted the grouping of samples based on similarities in their protein phosphorylation profiles, which aligned consistently with their respective experimental groups.

Within the dataset of differentially phosphorylated proteins, Abcb1a, Abcc5, and Gsr—genes known to be directly or indirectly associated with the NRF2-Keap1 pathway due to their roles in oxidative stress response, cytoprotective mechanisms, or interactions with related signaling cascades—were found to be deregulated. Specifically, one phosphorylation site was hypophosphorylated in each of these proteins. A full list of all deregulated phosphosites is provided in the Proteome Xchange Consortium via the JPOST partner repository.

To characterize in detail the altered hippocampal phosphoproteostatic target profile, a functional analysis of the affected biological functions was performed. The altered phosphopattern was associated with proteins significantly enriched in GO terms related to cellular components and molecular functions. Functional enrichment analysis based on GO cellular component terms identified altered proteins related to synaptic and axonal structures, highlighting clusters such as “postsynaptic density,” “asymmetric synapse,” “neuron-to-neuron synapse,” “postsynapse,” “axon,” “synapse,” “neuron projection,” “cell junction,” “plasma membrane-bounded cell projection,” and “cell projection” (Fig. 7D). Finally, when analyzing enriched GO terms related to molecular function, regulatory processes emerged, including “calmodulin binding,” “GTPase regulator activity,” “nucleoside-triphosphatase regulator activity,” “actin binding,” “phospholipid binding,” “cytoskeletal protein binding,” “protein kinase binding,” “kinase binding,” “enzyme regulator activity,” and “enzyme binding” (Fig. 7E).

Therefore, phosphoproteome analyses confirms NRF2 loss rewires hippocampal signaling with dysregulated phosphorylation concentrated in synaptic/axonal compartments and regulatory functions (calmodulin/actin/phospholipid binding; GTPase/kinase regulation), with site-specific directionality - including single hypophosphorylated sites on Abcb1a, Abcc5, and Gsr - implicating altered phosphorylation control as a key facet of the *Nfe2l2*$^{-/-}$ phenotype.

3.3.6. Western blot validation confirms oxidative and astroglial alterations and reveals tau imbalance in the hippocampus of Nfe2l2$^{-/-}$ *mice*

To validate the proteomic and phosphoproteomic findings, a subset of DEPs was selected for confirmation by Western blot. Candidate proteins were chosen based on several criteria, including the availability of high-quality, commercially validated antibodies suitable for Western blot analysis, their strong association with significantly enriched GO terms, and their relevance to key biological pathways identified in the dataset.

As an initial step, we examined components and mediators of the oxidative stress response and oxidative damage products. Statistical analysis using Student's t-test revealed a significant increase in 8-OHdG ($p = 0.004$) and MDAL ($p = 0.05$) levels in *Nfe2l2*$^{-/-}$ mice compared to WT controls, while reduced levels of GSTM2 ($p = 0.0002$) were reported in *Nfe2l2*$^{-/-}$ animals when compared to WT animals. In contrast, no significant differences were observed in the levels of other tested oxidative stress-related proteins or adducts, including 4-HNE ($p = 0.76$) and GSR ($p = 0.29$) (Fig. 8A).

Additionally, guided by transcriptomic data highlighting astrocytic involvement and structural changes in neuronal and glial projections observed in phosphoproteomic analysis, we analyzed a set of proteins representing distinct astrocyte components. While no significant differences were observed in ALDH1L1 ($p = 0.06$), GFAP ($p = 0.065$), *p*-GFAP ($p = 0.33$), YKL40 ($p = 0.65$) and VIM ($p = 0.75$) levels, both AQP4 ($p = 0.005$) and GFAP-C-terminal ($p = 0.0004$) were significantly upregulated in *Nfe2l2*$^{-/-}$ mice compared to WT animals (Fig. 8B).

In line with our research objectives, we also examined the expression of proteins related to tau physiology in the hippocampus of 3-month-old mice. No significant changes were observed in tau phosphorylation-associated proteins, such as GSK3-α/β ($p = 0.25$), GSK3β-*p*-Ser9 ($p = 0.77$) and p38 ($p = 0.09$), when compared between groups. However, total tau levels (TAU-5) were significantly reduced in *Nfe2l2*$^{-/-}$ mice compared to WT animals ($p = 0.046$), as determined by Student's t-test. To further explore this finding, we evaluated specific tau isoforms, showing decreased levels of 4R-tau ($p = 0.018$) and increased levels of 3R-tau ($p = 0.0002$) in *Nfe2l2*$^{-/-}$ mice when compared to WT animals. In consequence, in *Nfe2l2*$^{-/-}$ animals, an increased 3R/4R tau ratio in *Nfe2l2*$^{-/-}$ animals is reported when compared to WT animals ($p = 0.0001$), suggesting that the loss of NRF2 skews tau isoform expression toward the 3R isoform, disrupting the normal balance. In contrast, phosphorylation of tau at Ser-422, assessed using an anti-phospho-Ser-422 antibody, did not show significant differences between groups ($p = 0.13$) (Fig. 8C).

4. Discussion

4.1. Modulation of Tau seeding and spreading by NRF2 lack in 3-month of Nfe2l2$^{-/-}$ *animals hippocampus*

In this study, we investigated the early-stage molecular consequences of NRF2 deficiency in the hippocampus of mice and their potential implications for seeding and spreading of tau pathology. Given NRF2's critical role in maintaining redox homeostasis and regulating cellular defense mechanisms, we hypothesized its absence may create a permissive environment accelerating and enhancing the initiation and propagation of pathological tau. This is particularly relevant in the context of tau seeding and spreading, key events in the progression of sporadic tauopathies [68]. We evaluated how the NRF2-associated altered pathways influence the development of a sporadic-like neurodegenerative disease phenotype, with a specific focus on the mechanisms of tau seeding and spreading, as observed in AD and other tauopathies [35–39,42]. To this end, *Nfe2l2*$^{-/-}$ and WT mice were inoculated with AD human p-tau-enriched fractions directly into the hippocampus. After three months, the animals were sacrificed, and brain tissue was analyzed to assess tau accumulation in the injected region.

Our results reveal a surprising, yet robust and significant lower

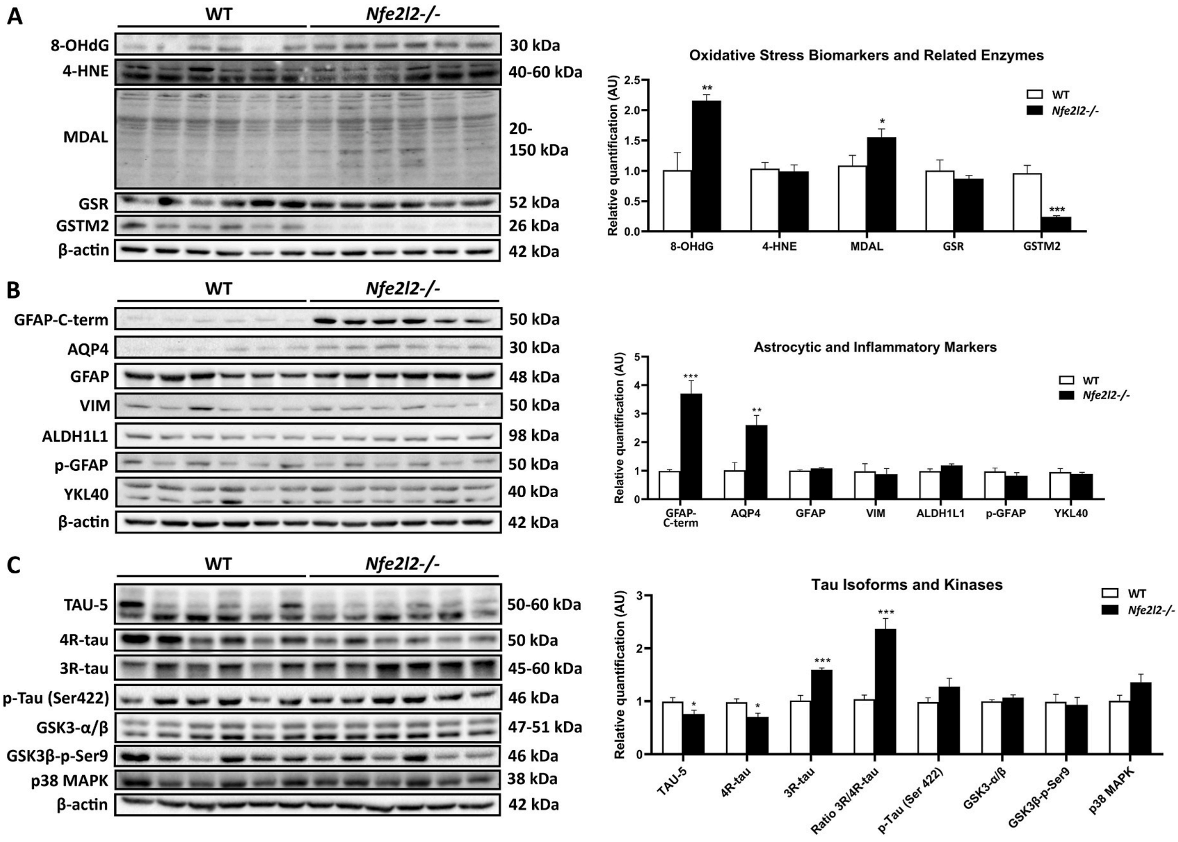

Fig. 8. Pathway-specific Western blot profiling of oxidative stress, inflammatory, and tau-related proteins in the hippocampus of *Nfe2l2*$^{-/-}$ versus WT mice. Graphical representation of protein levels and corresponding Western blot images. Proteins are grouped according to their associated pathways: **(A)** oxidative stress biomarkers and related enzymes; **(B)** astrocytic and inflammatory markers; and **(C)** tau isoforms and kinases. Statistical significance was defined as *$p < 0.05$, **$p < 0.01$, and ***$p < 0.001$.

amount of p-tau in the *Nfe2l2*$^{-/-}$ model compared to WT mice. WT mice exhibited similar levels and distribution according to what we observed previously using the same brain extracts inoculated in the same coordinates [35–39]; where we also demonstrated that tau obtained from different tauopathies [AD, Frontotemporal dementia (FTD), Globular glial tauopathy (GGT), Aging-related tau astrogliopathy (ARTAG), and Argyrophilic grain disease (AGD)] accumulates in WT animals independently of age and is capable of seeding and spreading from 1 month to 12 months at different incubation times [35–39]. Accordingly with these studies, in this work, in WT animals phospho-tau deposits were present and had expanded throughout the hippocampus, where they were detected in both neurons and their projections, as previously reported. Aggregates were mainly found in neurons, forming cap-like or comma-shaped structures, reminiscent of coiled bodies in human tauopathies. However, *Nfe2l2*$^{-/-}$ animals showed only a few phospho-tau deposits in the hippocampal region, and in some cases, none were detected.

In the corpus callosum, aggregates were present in both models, although they were less abundant in the Nfe2l2-/- model. Phospho-tau deposits were predominantly located perinuclearly or along cellular processes in oligodendrocytes, often forming cap-like or comma-shaped structures, as it has been previously reported [38,39,69].

In both models, no phospho-tau deposits were detected in microglia in any region. Likewise, phospho-tau accumulation in astrocytes was not observed, in agreement with previous reports that such inclusions are restricted to ARTAG-inoculated animals [39,69].

Based on all these data and observations, the seeding and spreading capacity in *Nfe2l2*$^{-/-}$ animals is more restricted and lower than in WT animals, affecting the same cell populations. However, this phenomenon is not unique to this model; similar differences in pathological progression have previously been reported in other conditions, such as in inoculated newborn WT animals [42]. In this last work, we postulated that differences in tau seeding between newborns and young adults may be related to the ratio of 3R-tau to 4R-tau, the shift toward 4R-tau predominance in adults, and the immaturity of neural connections in newborn mice [42]. This is similar to what we have observed in the *Nfe2l2*$^{-/-}$ model, in which 3R-tau levels are increased and 4R-tau levels are decreased, thereby modifying the 3R-tau/4R-tau ratio in the same manner as occurs in newborn animals. In addition, seeding and spreading are also regulated by the total amount of tau protein present in the host animal, and do not occur when the *Mapt* gene is absent, as we demonstrated previously [35]. It reinforces the importance of significantly downregulated total tau levels in impairing seeding and spreading mechanisms in *Nfe2l2*$^{-/-}$ model.

While WT mice exhibited the expected pattern, *Nfe2l2*$^{-/-}$ animals showed a protection against for seeding and spreading. Currently, there are no studies on the role of NRF2 in the seeding and spreading mechanisms of pathological tau in inoculated mouse models of “sporadic” tauopathies to compare our results with. Previous studies have used *Nfe2l2*$^{-/-}$ mouse model mixed with transgenic animal models of different tau-related disorders to evaluate the effect of NRF2 deficiency in AD models and its implications for the disease. In addition, and relevantly, most of these studies focus on advanced or late stages of disease-like phenotypes, whereas our work investigates tau propagation in young adult animals without a genetically altered AD background.

This distinction is crucial, as the timing of pathology onset and the maturity of the cellular environment may significantly influence the mechanisms of tau seeding and spreading. For instance, double transgenic mice carrying APP and MAPT mutations in a NRF2 WT (NRF2-WT) background died prematurely at around 14 months of age due to motor deficits and a terminal spinal deformity, while APP/MAPT-*Nfe2l2*$^{-/-}$ mice died approximately 2 months earlier; associating NRF2 deficiency with exacerbated astrogliosis and microgliosis, as evidenced by increased levels of GFAP, IBA1, and CD11b in this AD-like background [28,31,70]. Similarly, other works point out that the ablation of NRF2 in APP/PS1 mice exacerbates spatial learning and memory deficits as well as AD-like pathology, correlating with increased oxidative damage and neuroinflammatory processes [28,31,70]. In contrast, in tauopathy models such as P301S mice, loss of this transcription factor accelerates neurodegeneration without increasing total or phosphorylated tau levels compared to controls [71].

Thus, when comparing these “sporadic” and “genetic” models, it is important to consider both the nature and timing of the pathological insults applied. In our study, inoculated animals are subjected to a specific and relatively mild insult at the time of inoculation, in contrast to transgenic models, which are exposed to a continuous and more severe pathological burden from birth, progressively worsening with age. For example, *Nfe2l2*$^{-/-}$ mice do not initially present with tau pathology and are inoculated at three months of age, allowing for the study of tau propagation in a more temporally controlled manner. By comparison, models such as APP/MAPT-*Nfe2l2*$^{-/-}$ experience persistent amyloid and tau pathology from early developmental stages, which may lead to compounded or synergistic effects on neurodegeneration, depending on the transgenes involved.

After observing these differences in tau accumulation between *Nfe2l2*$^{-/-}$ and WT mice, we next sought to characterize the basis of the protection of the inoculated region at 3 months of age using different -omics. This approach was aimed at uncovering the underlying mechanisms responsible for the distinct outcomes, thereby providing insights into how NRF2 deficiency influences the cellular and molecular environment that governs tau seeding and spreading in our model.

4.2. NRF2 loss establishes a latent pro-vulnerable transcriptional state in hippocampal tissue based on reduced anti-inflammatory and antioxidant mechanisms

We explored the impact of NRF2 deficiency on the hippocampus by performing transcriptomic profiling of hippocampal tissue from *Nfe2l2*$^{-/-}$ and WT mice. This analysis aimed to uncover the gene expression changes driven by the loss of NRF2 and to provide insight into its broader regulatory role in hippocampal biology. The transcriptomic analysis reveals significant insights into the role of NRF2 in regulating gene expression and maintaining cellular homeostasis. Upregulated genes were enriched in pathways related to the immune response and metabolic processes, consistent with previous studies that involved silencing NRF2 [28,72]. In contrast, down-regulation profile is linked to genes implied in functional clusters such as “oxidative stress response” and “redox pathways”, resembling down-regulated pathways observed in cardiac tissue, where transcriptional signature of mitochondrial, and redox and metabolic pathways, were found altered [73].

It is important to note published transcriptomic studies in *Nfe2l2*$^{-/-}$ animals are limited in number, often lack a specific focus on *Nfe2l2*$^{-/-}$ models or brain regions, and frequently involve animals of varying ages. Most studies reporting transcriptomic changes in *Nfe2l2*$^{-/-}$ mice do so in the context of additional genetic mutations associated with neurodegenerative diseases [74]. However, the absence of NRF2-mediated regulation exacerbates gene expression and other molecular alterations replicating pathway alterations found in human elderly and AD brains, such as oxidative damage, disrupts redox homeostasis and neuroinflammation [28,31].

Consistent with these findings, our validated data also supports the notion of an impaired oxidative stress response in the absence of NRF2 by q-PCR. Specifically, we observed decreased mRNA expression levels of key detoxification and antioxidant effectors such as catalase (*Cat*), glutathione reductase (*Gsr*), glutathione s-transferase μ 1 (*Gstm1*), superoxide dismutase 2 (*Sod2*), sulfiredoxin 1(*Srxn1*) and nitric oxide synthase 1 (*Nos1*). In addition, NRF2-Keap1 regulatory pathway was also affected by the lack of *Nfe2l2* gene, showing decreased levels of NRF2 (*Nfe2l2*), Kelch Like ECH Associated Protein 1 (*Keap1*) and (NAD (P)H Quinone Dehydrogenase 1 (*Nqo1*). The downregulation of these genes suggests a shift away from antioxidant and cellular defense mechanisms, which may indicate increased basal oxidative stress vulnerability, impaired redox homeostasis, and reduced cytoprotection, confirmed by oxidative-stress derived modifications. These data are according to previous results reported when studying the regulatory mechanisms of NRF2 protein not applying -omic approaches in other organs, where changes are observed in antioxidant mechanisms, inflammatory mediators and/or impaired mitochondria energy metabolism [75,76]. In addition, downregulation is mainly observed in genes coding for receptors for anti-inflammatory mediators. Interestingly, while classic pro-inflammatory and innate immune genes (*Il1b*, *Il6*, *Tnfa*, *Cxcl10*, *Ifnb1*, *Tlr4*, *Tlr7*) and cathepsins (*Ctsc*, *Ctsg*, *Ctss*) showed no significant changes, suggesting the absence of a broad inflammatory activation, we observed a significant downregulation of the expression of *Il10ra*, *Il10rb*, *Tgfb2*, and *Tnfrsf1a*. *Il10ra* and *Il10rb* encode receptors for IL-10 and are typically associated with anti-inflammatory signaling [77], while *Tgfb2* is another potent immunosuppressive cytokine [78]. In contrast, *Tnfrsf1a*, which encodes a receptor for TNF-α, may have pro-inflammatory or anti-inflammatory outcomes depending on various factors, including the cell type, the presence of other signaling molecules, and the dose of TNF-α [79].

We also observed a significant increase in *Aqp4* expression, suggesting enhanced astrocyte reactivity and potential changes in water homeostasis or blood–brain barrier dynamics [80]. In contrast, the expression of *Inpp5d*, *S100b*, and *Ptgs2* (COX-2) was significantly reduced. The downregulation of *Inpp5d*, a negative regulator of microglial activation, may indicate a shift toward a more proinflammatory or dysregulated microglial state [81]. Meanwhile, decreased levels of *S100b* and *Ptgs2*, both of which are commonly upregulated during glial activation and neuroinflammation [82,83], may reflect a non-classical or suppressed inflammatory profile in glial cells.

The altered expression of these genes may indicate a selective or regulated immune modulation, where anti-inflammatory pathways are engaged alongside components of pro-inflammatory signaling, reflecting a complex or transitional immune state rather than full immune quiescence [84–89]. Our results confirm previous studies showing that NRF2 plays an important role in the anti-inflammatory and antioxidative effects under certain conditions [22].

In addition, at three months of age, transcriptomic analyses revealed no impairments or alterations in autophagy-related pathways. This contrasts with previous reports in which the same model was examined at six months of age, showing changes in autophagy [90]. However, the study that specifically characterized the *Nfe2l2*$^{-/-}$ model in relation to autophagy and tau phosphorylation presented methodological inconsistencies, particularly regarding the age of the compared animal groups and the number of subjects used [90]. Although we observed reduced tau propagation in the *Nfe2l2*$^{-/-}$ model inoculated at 3-month-old, this effect was not associated with basal changes in the expression of genes encoding selective autophagy cargo receptors such as *Sqstm1*/p62 or *Npd52*. This suggests that the reduction in tau spread is unlikely to be driven by transcriptional upregulation of these pathways. Notably, previous work has shown that *Sqstm1*-mediated regulation of tau pathology primarily depends on protein-level interactions and autophagic flux rather than changes in gene expression [91]. Therefore, the absence of transcriptional alterations in the autophagy pathway in our model does not preclude NRF2-dependent effects on tau handling mediated through post-transcriptional mechanisms, altered autophagic efficiency, or lysosomal dysfunction. However, broader NRF2-related changes in inflammation, glial reactivity, or neuronal network integrity may indirectly restrict tau uptake and propagation, thereby contributing to the reduced tau pathology observed in NRF2-deficient animals.

Finally, one of the key consequences of NRF2 deficiency in the brain is impaired glucose and energy metabolism. NRF2 supports cellular energetics not only by maintaining mitochondrial function and redox balance but also by regulating the expression of genes involved in metabolic substrate transport and utilization [6,92]. In our study, we observed a significant downregulation of *Slc2a1* and *Slc16a7*, which encode the glucose transporter GLUT1 and the monocarboxylate transporter MCT2, respectively. *Slc2a1* is essential for glucose transport across the blood–brain barrier and into astrocytes and neurons, while *Slc16a7* facilitates neuronal uptake of lactate and pyruvate—key alternative energy substrates supplied by astrocytes [93]. The concurrent reduction in these transporters suggests a compromised capacity for both glucose uptake and lactate shuttling, leading to reduced metabolic flexibility in NRF2-deficient brains. This may render neurons more vulnerable to oxidative stress and energetic failure, particularly under conditions of increased demand or injury. These findings align with previous reports implicating NRF2 in the regulation of metabolic adaptation and support the hypothesis that NRF2 loss impairs not only antioxidant defense but also neuronal energy homeostasis [94].

All of this may suggest that NRF2 deficiency creates a low-defense basal state, that, while compensated and stable early in life, becomes increasingly vulnerable to proinflammatory activation and autophagy disruption with aging or environmental exposure—particularly as oxidative stress products begin to rise significantly beyond six months of age [17,95]. In consequence, this early modified inflammatory profile must not be considered proinflammatory, but an altered inflammation profile, as it doesn't match with previous results reported in pathological conditions of neurodegeneration in other mice models [44,45,96], that reinforces a latent pro-vulnerable transcriptional state in hippocampal tissue based on reduced anti-inflammatory and antioxidant mechanisms.

4.3. *Phosphoproteomic profiling reveals early neuroglial imbalance in the NRF2-deficient hippocampus: evidence of astrocytic activation and cytoskeleton reshaping*

To complement the transcriptomic analysis and gain deeper insight into translational and post-translational regulatory mechanisms influenced by NRF2 deficiency, we performed phosphoproteomic profiling of hippocampal tissue from *Nfe2l2*$^{-/-}$ and WT mice. Functional analysis indicated that downregulated proteins are primarily associated with mitochondrial function -including energy metabolism and ROS regulation - as well as components of the synaptic vesicle system. In contrast, upregulated proteins were linked to inflammatory responses and structural elements of both neurons and glial cells. These findings are consistent with our transcriptomic results and also with previous proteomic studies in skeletal muscle, which similarly reported alterations in antioxidant defenses and mitochondrial function in the context of NRF2 deficiency [97,98], and others performed in cell cultures of endothelial cells that also overlap in proteins belonging to clusters related to cytoskeleton, angiogenesis, or inflammation [99].

Given NRF2's role in redox homeostasis and cellular defense, we hypothesized that its absence would alter the phosphorylation landscape, affecting proteins involved in metabolic regulation, inflammation, cytoskeletal organization, and neuronal communication. To our knowledge, no previous studies have applied a phosphoproteomic approach to investigate NRF2 deficiency in the brain, making this analysis a novel contribution to the field. The phosphoproteomic profiling offers a complementary perspective to transcriptomic data, revealing functional consequences of NRF2 loss that may not be detectable at the gene expression level. This approach enables the identification of early, post-translational molecular imbalances that could precede overt neurodegenerative phenotypes and provides deeper insight into the regulatory networks disrupted by NRF2 deficiency.

Together, these phosphoproteomic findings underscore a broader role for NRF2 in maintaining hippocampal homeostasis beyond its classical antioxidant function. The disruption of phosphorylation networks central to synaptic integrity and neuronal signaling suggests that NRF2 loss may set the stage for functional decline and heightened vulnerability to neurodegenerative processes, particularly in the context of AD or tauopathies. These results complement earlier transcriptomic and proteomic data and support the hypothesis that NRF2 acts as a key modulator of neuronal resilience, whose absence may accelerate the onset or progression of synaptic pathology observed in AD.

To validate key findings from the phosphoproteomic analyses, we performed Western blotting on some of selected targets or molecules related to the altered pathways. This approach allowed us to confirm changes at the protein level and assess the functional relevance of identified molecular alterations in NRF2-deficient hippocampal tissue. The up-regulated proteins are consistent with transcriptome results, demonstrating changes in inflammatory clusters as well as in neuronal and glial structural components. Specifically, validated proteins indicated increased levels of the GFAP isoforms expressing C-terminal canonical tail, that influences intermediate filament assembly toward more stable and bundled cytoskeletal networks, consistent with astrocyte maturation and reactive remodeling. This shift is associated with reduced cytoskeletal plasticity, enhanced cellular rigidity, and a transition toward a differentiated, structurally supportive astrocyte phenotype, commonly observed during gliosis and tissue stabilization responses [100–102]. This shift likely reflects an adaptive response to cellular stress, enabling astrocytes to provide increased structural support and maintain tissue homeostasis in the face of metabolic imbalance or synaptic perturbation, even in the absence of overt inflammatory signaling [103,104]. In addition, altered GFAP levels can lead to changes in astrocyte shape, potentially affecting their interactions with neighboring cells and blood vessels [105,106].

Moreover, levels of aquaporin-4 protein (AQP4), the principal water channel in the brain and predominantly localized to astrocytes [107], were also increased, signifying astrocytic responses to altered water, ionic, or vascular demands - most often reflecting reactive gliosis, BBB stress, or tissue remodeling rather than simple changes in cell number.

These changes may translate into a specific proliferation of astrocytic populations [108], indicating a different and characteristic glial profile for *Nfe2l2*$^{-/-}$ animals. Specifically, the concomitant increase in GFAP and AQP4 indicates reactive astrocyte remodeling, consistent with enhanced structural support and water/ion homeostatic responses to CNS stress in this model.

Furthermore, 8-oxoguanine DNA glycosylase (8-OHdG), a marker of oxidative DNA damage, and MDAL, a marker of oxidative protein damage, were both increased, while GSTM2, a glutathione S-transferase isoform involved in the detoxification of reactive oxygen species–derived byproducts and the maintenance of cellular redox balance, was decreased in *Nfe2l2*$^{-/-}$ animals. These alterations are partially consistent with previous reports using NRF2 silencing, supporting the notion that NRF2 deficiency contributes to impaired antioxidant defense and enhanced oxidative stress [72]. In contrast, changes in other antioxidant elements, structural or synaptic components evaluated did not suffer significant changes.

Together, the upregulation of GFAP and aquaporin-4 suggests that astrocytes in *Nfe2l2*$^{-/-}$ mice may be in a pre-inflammatory or “alert” state, attempting to maintain homeostasis in response to redox and metabolic stress. This aligns with the broader idea that NRF2 deficiency does not cause immediate pathology but instead establishes a vulnerable, dysregulated baseline that could accelerate neurodegenerative processes under further insult or aging [109].

We next sought to examine whether NRF2 deficiency extends to the regulation of tau, a key cytoskeletal protein implicated in AD and tauopathies neurodegeneration. Tau plays a critical role in stabilizing microtubules in neurons and also glial cells, and its function is tightly controlled by site-specific phosphorylation. Dysregulation of tau phosphorylation is a hallmark of Alzheimer's disease, leading to its detachment from microtubules, aggregation, and toxicity [110]. To explore whether NRF2 deficiency contributes to tau-related dysfunction, we assessed total tau levels, the expression of major isoforms (3R and

4R-tau), and the status of key tau kinases, including GSK3-α/β and MAPKs [111]. This targeted analysis was designed to determine whether the early cytoskeletal disruptions revealed by omics approaches are accompanied by molecular signatures of tau dysregulation, thereby potentially linking NRF2 loss to the onset of tauopathy.

Our results indicated that, at 3 months of age, total tau levels are altered in the hippocampus of *Nfe2l2*$^{-/-}$ animals, along with changes in tau isoform protein levels. Specifically, total tau and 4R-tau isoform levels were reduced, while the expression of the 3R tau isoform was increased. In contrast, phosphorylated tau forms, as well as key tau-regulating kinases such as GSK3-α/β and MAPKs, remain unchanged. The reduction in total tau may reflect an adaptive or compensatory mechanism in response to early cytoskeletal stress or cellular adaptation. The increase in 3R-tau could reflect early post-transcriptional or post-translational adjustments in microtubule dynamics, potentially linked to compensatory responses to cytoskeletal stress or altered RNA splicing regulation in the absence of NRF2. This isoform shift is particularly striking, as 3R-tau is predominantly expressed during early brain development, when dynamic microtubule remodeling is essential for neurite outgrowth and axonal guidance [112–114]. In healthy adult mouse brains, tau expression transitions toward the 4R isoform, which has greater microtubule-binding affinity and contributes to structural stabilization [112–115]. The upregulation of 3R-tau together with the concomitant downregulation of 4R-tau isoforms in adulthood in the *Nfe2l2*$^{-/-}$ model strongly suggests a developmentally immature and dysregulated tau isoforms expression profile. This aberrant pattern indicates that NRF2 deficiency profoundly disrupts the normal temporal regulation of tau isoform switching, a process that is critical for neuronal maturation and function.

Beyond its developmental implications, the increased 3R/4R tau ratio could compromise microtubule stability and axonal integrity [116]. While 3R-tau promotes cytoskeletal flexibility, excessive expression in mature neurons may lead to reduced microtubule binding and impaired support for axonal transport or synaptic maintenance. In the context of NRF2 loss - where transcriptomic and phosphoproteomic data already point to oxidative stress, anti-inflammatory dysfunction, and synaptic vulnerability - this altered isoform profile could further destabilize the neuronal cytoskeleton, increasing structural plasticity at the expense of stability, creating a vulnerable baseline that may exacerbate physiological problems under additional stressors or aging, such as vacuolar leukoencephalopathy [23].

Importantly, the lack of change in phosphorylated tau or kinase activity at this early stage supports the notion that NRF2 deficiency may not directly promote tau aggregation or hyperphosphorylation. It is contrary to the observed by other authors, that at six months of age, showed increased levels of total tau and phosphorylated forms in a *Nfe2l2*$^{-/-}$ model. However, as we mentioned before, the study presents methodological inconsistencies, particularly regarding the age of the compared animal groups and the number of subjects used [90]. Supporting our findings, studies in specific tauopathy models such as P301S transgenic mice—which overexpress mutant human tau—have shown that NRF2 loss accelerates neurodegenerative phenotypes, including hind-limb paralysis and cognitive decline, without further increasing total tau or phosphorylated tau levels in the brain compared to P301S mice with intact NRF2 expression [71]. This reinforces our data, as suggests that the exacerbation of disease symptoms associated with NRF2 deficiency is not driven by increased tau accumulation or phosphorylation alone but may instead result from heightened broader impairments in cellular resilience.

Finally, in our study, changes observed at the transcriptomic level did not consistently overlap with proteomic alterations. This discrepancy likely reflects layers of post-transcriptional and translational regulation, differences in protein stability, and the distinct technical sensitivities of RNA-seq versus mass spectrometry. Such findings underscore that transcript abundance does not necessarily predict protein levels, highlighting the need to integrate both datasets for a comprehensive view of cellular regulation.

4.4. Molecular landscape impairs seeding and spreading processes of tau protein

Based on these premises, and considering our results, our findings suggest that NRF2 deficiency results in a hippocampal environment that is less permissive to tau pathology propagation, possibly due to a delayed maturation of molecular and cellular pathways involved in tau seeding and spreading. The observed reduction in total tau and 4R-tau, the predominance of 3R-tau, and plastic astrocytic profiles in *Nfe2l2*$^{-/-}$ mice resemble features of early developmental stages, which are known to resist tau propagation, as we previously observed [35,42]. Combined with the sustained downregulation of antioxidant and anti-inflammatory responses, typically enhanced by NRF2, this altered state may contribute to a form of resistance against the templated spread of pathological tau. As these animals age, it is conceivable that their molecular profile will shift toward a more mature and permissive state, potentially facilitating tau propagation or even enhancing it through cumulative oxidative damage. However, direct experimental validation of this hypothesis is not feasible due to the development of vacuolar leukoencephalopathy in *Nfe2l2*$^{-/-}$ mice beyond 6 months of age [23]. Therefore, while our current data support a protective, immature-like phenotype at 3 months, the long-term consequences of NRF2 deficiency on tau propagation remain unresolved and warrant investigation using alternative approaches, such as conditional knockout models.

Altered inflammatory components reported in this study may also help explain the impairments in tau propagation observed in our model. This interpretation is consistent with previous work showing that, in the presence of tau pathology, NRF2 activation attenuates secondary inflammatory responses, whereas NRF2 deficiency exacerbates glial activation when tau is present [117]. In particular, this study demonstrated that loss of NRF2 enhances microgliosis and astrogliosis in response to neuronal tau expression, supporting a role for NRF2 as a modulator of tau-induced neuroinflammation. Importantly, however, that study employed a lentiviral-induced tau expression model and did not perform direct quantification of tau burden or aggregation. Therefore, while NRF2 deficiency was associated with exacerbated inflammatory responses, its impact on tau accumulation or propagation per se could not be assessed in that context. In contrast, our tau inoculation paradigm directly evaluates tau seeding and spreading, suggesting that basal altered inflammatory or glial responses in NRF2-deficient animals may differentially influence tau propagation dynamics, potentially leading to reduced detectable tau pathology despite heightened inflammatory reactivity.

In addition, previous studies further support our findings by demonstrating that NRF2 deficiency profoundly affects glial cellular components in the hippocampus. Specifically, loss of NRF2 reduces adult hippocampal neurogenesis and promotes a shift toward glial phenotypes, resulting in an altered cellular composition of the neurogenic niche that may influence how tau seeds are taken up, cleared, or propagated within the brain [118]. In particular, changes in the relative proportions of neurons and glial cells could modify extracellular matrix composition, phagocytic capacity, and cytokine signaling profiles—factors that are known to modulate tau internalization, intercellular transfer, and prion-like propagation. Collectively, these alterations provide a plausible mechanistic link between NRF2-dependent regulation of hippocampal cellular homeostasis and the reduced tau pathology observed in NRF2-deficient animals following tau inoculation.

The present work offers comprehensive multi-omic insights into NRF2 function in the hippocampus, though several limitations should be acknowledged. Although extensive, it is limited by the fact that all analyses were performed in bulk hippocampus from 3-month-old mice with modest cohort sizes, which limits power—particularly for sex interactions—and obscures cell-type–specific effects. Second, the multi-omics findings (DEGs, WGCNA modules, DEPs, phosphosites) are correlative; we did not include causal tests (e.g., NRF2 re-expression or cell-type–restricted manipulations, kinase activity assays, autophagy flux) or functional readouts (electrophysiology) to link molecular changes to circuit or organismal phenotypes. Third, cross-platform thresholds and antibody availability introduce selection bias, and several targets were near detection limits, so validations cover only a subset of candidates. Fourth, pathway inferences (immune/complement, amino-acid/vitamin metabolism, PI3K–Akt–mTOR) derive from enrichment analyses without orthogonal confirmation (e.g., complement activity, metabolomics). Fifth, phosphosite directionality was site-specific and not mapped to upstream kinases or phosphorylation stoichiometry, constraining mechanistic interpretation. Finally, tau-seeding experiments used a single inoculum, site, and time point with semi-quantification in one region. These caveats temper generalization beyond the hippocampus and support the need for future longitudinal, cell-type–resolved, and interventional studies. Despite these constraints, the convergent multi-omics and validation data present a coherent, biologically plausible framework implicating NRF2 in hippocampal immune–metabolic regulation, synaptic remodeling, and tau susceptibility, providing a solid foundation for mechanistic follow-up and translational exploration.

In the absence of prior studies exploring NRF2's role in tau inoculation models of “sporadic” tauopathies, these results provide novel evidence linking NRF2 activity to the molecular readiness of the brain to support tau propagation. This raises the possibility that NRF2 not only modulates oxidative stress and inflammation but also influences the tau proteostasis and cellular maturity necessary for efficient seeding and spreading. In addition, our results highlight the potential of therapies that mimic the immature hippocampal environment, which appears resistant to tau propagation. Such interventions could involve shifting tau isoform expression toward 3R-tau or modulating astrocyte maturation to sustain a non-permissive state. While still speculative, this approach may offer a novel direction for slowing the spread of tau pathology, particularly in early or preclinical stages of disease.

5. Conclusion

In this study, we demonstrate that NRF2 deficiency results in a hippocampal environment that is less permissive, or even preventive, to the seeding and spreading of pathological tau following inoculation. This resistance is associated with a molecular and cellular profile resembling an immature brain state - characterized by reduced total tau levels, a predominance of 3R tau, immature astrocytic markers, and sustained downregulation of antioxidant and anti-inflammatory responses. These features collectively suggest that NRF2 plays a previously unrecognized role in shaping the permissiveness of the brain to tau pathology.

Our findings highlight the importance of the host environment in modulating tau propagation, beyond the presence of pathological tau itself. They also underscore the need to consider the timing and nature of disease insults when interpreting outcomes across different tauopathy models. Although long-term investigation is limited by the onset of vacuolar leukoencephalopathy in aged *Nfe2l2*$^{-/-}$ mice, our results provide a foundation for future studies using inducible or cell-specific NRF2 models to dissect the temporal dynamics of this regulatory pathway.

Overall, this work adds a new dimension to our understanding of sporadic tauopathies by linking NRF2 signaling not only to neuroprotection but also to the molecular readiness of the brain to support tau seeding and spreading. These insights open new avenues for therapeutic strategies aimed at modulating the host environment to slow or prevent the progression of tau-related neurodegeneration.

Availability of data and material

All data generated or analyzed during this study are included in this published article and its supplementary information files.

CRediT authorship contribution statement

Yaiza López-Sampere: Data curation, Formal analysis, Investigation, Methodology, Validation, Visualization. **Pol Mengod Soler:** Data curation, Formal analysis, Visualization. **Sergio Roca-Pereira:** Investigation, Methodology. **Antonia Vinyals:** Investigation, Methodology. **Xoel Mato-Blanco:** Data curation, Formal analysis. **Marta Vela-Martínez:** Investigation, Methodology. **Farida Dakterzada:** Investigation, Methodology. **Leila Romero:** Investigation, Methodology. **Enrique Santamaría:** Data curation, Formal analysis, Methodology. **Joaquín Fernández-Irigoyen:** Data curation, Formal analysis, Methodology. **Isidro Ferrer:** Data curation, Visualization, Writing – original draft. **Mónica Povedano:** Data curation, Formal analysis, Project administration. **José Antonio Del Rio:** Data curation, Visualization, Writing – original draft, Writing – review & editing. **Gabriel Santpere:** Data curation, Formal analysis, Methodology. **Manuel Portero-Otín:** Data curation, Visualization, Writing – original draft, Writing – review & editing. **Gerard Piñol-Ripoll:** Funding acquisition, Supervision, Visualization, Writing – original draft, Writing – review & editing. **Pol Andrés-Benito:** Conceptualization, Data curation, Formal analysis, Funding acquisition, Project administration, Supervision, Visualization, Writing – original draft, Writing – review & editing.

Declaration of competing interest

The authors declare that they have no known competing financial interests or personal relationships that could have appeared to influence the work reported in this paper: “NRF2 Deficit Prevents Pathologic Tau Seeding and Spreading in an Induced Tauopathy Mouse Model”.

Acknowledgments

MPO was supported by grants from the Instituto de Salud Carlos III (PI20/000155, PI23/00176), and PAB was supported by grants from the same governmental institution (CD23/00097). The project that gave rise to these results received the support of a fellowship to PMS from Fundación Ramón Areces. We want to particularly acknowledge patients and Biobank HUB-ICO-IDIBELL (PT20/00171) integrated in the ISCIII Biobanks and Biomodels Platform and Xarxa Banc de Tumors de Catalunya (XBTC) for their collaboration. We thank CERCA Programme/ Generalitat de Catalunya for institutional support.

Appendix A. Supplementary data

Supplementary data to this article can be found online at https://doi.org/10.1016/j.redox.2026.104068.

References

[1] D. Khaltourina, Y. Matveyev, A. Alekseev, F. Cortese, A. Ioviţă, Aging fits the disease criteria of the international classification of diseases, Mech. Ageing Dev. 189 (2020), https://doi.org/10.1016/j.mad.2020.111230.

[2] D.A. Johnson, J.A. Johnson, Nrf2 - a therapeutic target for the treatment of neurodegenerative diseases, Free Radic. Biol. Med. 88 (2015) 253–267, https://doi.org/10.1016/j.freeradbiomed.2015.07.147.

[3] C.J. Schmidlin, M.B. Dodson, L. Madhavan, D.D. Zhang, Redox regulation by NRF2 in aging and disease, Free Radic. Biol. Med. 134 (2019) 702–707, https://doi.org/10.1016/j.freeradbiomed.2019.01.016.

[4] C. López-Otín, M.A. Blasco, L. Partridge, M. Serrano, G. Kroemer, The hallmarks of aging, Cell 153 (2013) 1194, https://doi.org/10.1016/j.cell.2013.05.039.

[5] T.W. Kensler, N. Wakabayashi, S. Biswal, Cell survival responses to environmental stresses via the Keap1-Nrf2-ARE pathway, Annu. Rev. Pharmacol. Toxicol. 47 (2007) 89–116, https://doi.org/10.1146/ANNUREV.PHARMTOX.46.120604.141046.

[6] J.D. Hayes, A.T. Dinkova-Kostova, The Nrf2 regulatory network provides an interface between redox and intermediary metabolism, Trends Biochem. Sci. 39 (2014) 199–218, https://doi.org/10.1016/j.tibs.2014.02.002.

[7] T. Liu, Y.F. Lv, J.L. Zhao, Q.D. You, Z.Y. Jiang, Regulation of Nrf2 by phosphorylation: consequences for biological function and therapeutic implications, Free Radic. Biol. Med. 168 (2021) 129–141, https://doi.org/10.1016/j.freeradbiomed.2021.03.034.

[8] L. Baird, A.T. Dinkova-Kostova, The cytoprotective role of the Keap1-Nrf2 pathway, Arch. Toxicol. 85 (2011) 241–272, https://doi.org/10.1007/S00204-011-0674-5.

[9] T. Heurtaux, D.S. Bouvier, A. Benani, S. Helgueta Romero, K.B.M. Frauenknecht, M. Mittelbronn, L. Sinkkonen, Normal and pathological NRF2 signalling in the central nervous system, Antioxidants 11 (2022), https://doi.org/10.3390/ANTIOX11081426.

[10] M. Dodson, A. Anandhan, D.D. Zhang, L. Madhavan, An NRF2 perspective on stem cells and ageing, Frontiers in Aging 2 (2021), https://doi.org/10.3389/FRAGI.2021.690686.

[11] D. Matsumaru, H. Motohashi, The KEAP1-NRF2 system in healthy aging and longevity, Antioxidants 10 (2021), https://doi.org/10.3390/ANTIOX10121929.

[12] N. Kubben, W. Zhang, L. Wang, T.C. Voss, J. Yang, J. Qu, G.H. Liu, T. Misteli, Repression of the antioxidant NRF2 pathway in premature aging, Cell 165 (2016) 1361–1374, https://doi.org/10.1016/j.cell.2016.05.017.

[13] K.N. Lewis, E. Wason, Y.H. Edrey, D.M. Kristan, E. Nevo, R. Buffenstein, Regulation of Nrf2 signaling and longevity in naturally long-lived rodents, Proc. Natl. Acad. Sci. U. S. A. 112 (2015) 3722–3727, https://doi.org/10.1073/PNAS.1417566112.

[14] H. Zhang, K.J.A. Davies, H.J. Forman, Oxidative stress response and Nrf2 signaling in aging, Free Radic. Biol. Med. 88 (2015) 314–336, https://doi.org/10.1016/j.freeradbiomed.2015.05.036.

[15] A. Silva-Palacios, M. Ostolga-Chavarría, C. Zazueta, M. Königsberg, Nrf2: molecular and epigenetic regulation during aging, Ageing Res. Rev. 47 (2018) 31–40, https://doi.org/10.1016/j.arr.2018.06.003.

[16] S. Samarghandian, M. Nezhad, F. Samini, Preventive effect of safranal against oxidative damage in aged male rat brain, Exp. Anim. 64 (2015) 65–71, https://doi.org/10.1538/EXPANIM.14-0027.

[17] H.J. Tsay, P. Wang, S.L. Wang, H.H. Ku, Age-associated changes of superoxide dismutase and catalase activities in the rat brain, J. Biomed. Sci. 7 (2000) 466–474, https://doi.org/10.1007/BF02253362.

[18] I. Hajjar, S.S. Hayek, F.C. Goldstein, G. Martin, D.P. Jones, A. Quyyumi, Oxidative stress predicts cognitive decline with aging in healthy adults: an observational study, J. Neuroinflammation 15 (2018), https://doi.org/10.1186/S12974-017-1026-Z.

[19] B. Schöttker, K.U. Saum, E.H.J.M. Jansen, B. Holleczek, H. Brenner, Associations of metabolic, inflammatory and oxidative stress markers with total morbidity and multi-morbidity in a large cohort of older German adults, Age Ageing 45 (2016) 127–135, https://doi.org/10.1093/AGEING/AFV159.

[20] M. Baierle, S.N. Nascimento, A.M. Moro, N. Brucker, F. Freitas, B. Gauer, J. Durgante, S. Bordignon, M. Zibetti, C.M. Trentini, M.M.M.F. Duarte, T. Grune, N. Breusing, S.C. Garcia, Relationship between inflammation and oxidative stress and cognitive decline in the institutionalized elderly, Oxid. Med. Cell. Longev. 2015 (2015), https://doi.org/10.1155/2015/804198.

[21] N.G. Innamorato, A. Jazwa, A.I. Rojo, C. García, J. Fernández-Ruiz, A. Grochot-Przeczek, A. Stachurska, A. Jozkowicz, J. Dulak, A. Cuadrado, Different susceptibility to the parkinson's toxin MPTP in mice lacking the redox master regulator Nrf2 or its target gene heme oxygenase-1, PLoS One 5 (2010) 1–11, https://doi.org/10.1371/JOURNAL.PONE.0011838.

[22] S.S.S. Boyanapalli, X. Paredes-Gonzalez, F. Fuentes, C. Zhang, Y. Guo, D. Pung, C. L.L. Saw, A.N.T. Kong, Nrf2 knockout attenuates the anti-inflammatory effects of phenethyl isothiocyanate and curcumin, Chem. Res. Toxicol. 27 (2014) 2036–2043, https://doi.org/10.1021/TX500234H.

[23] A.F. Hubbs, S.A. Benkovic, D.B. Miller, J.P. O'Callaghan, L. Battelli, D. Schwegler-Berry, M. Qiang, Vacuolar leukoencephalopathy with widespread astrogliosis in mice lacking transcription factor Nrf2, Am. J. Pathol. 170 (2007) 2068–2076, https://doi.org/10.2353/ajpath.2007.060898.

[24] S. Tarantini, M.N. Valcarcel-Ares, A. Yabluchanskiy, Z. Tucsek, P. Hertelendy, T. Kiss, T. Gautam, X.A. Zhang, W.E. Sonntag, R. De Cabo, E. Farkas, M.H. Elliott, M.T. Kinter, F. Deak, Z. Ungvari, A. Csiszar, Nrf2 deficiency exacerbates obesity-induced oxidative stress, neurovascular dysfunction, blood-brain barrier disruption, neuroinflammation, amyloidogenic gene expression, and cognitive decline in mice, Mimicking the Aging Phenotype, Journals of Gerontology - Series A Biological Sciences and Medical Sciences 73 (2018) 853–863, https://doi.org/10.1093/GERONA/GLX177.

[25] M. Sandberg, J. Patil, B. D'Angelo, S.G. Weber, C. Mallard, NRF2-regulation in brain health and disease: implication of cerebral inflammation, Neuropharmacology 79 (2014) 298–306, https://doi.org/10.1016/j.neuropharm.2013.11.004.

[26] A. Cuadrado, Brain-protective mechanisms of transcription factor NRF2: toward a common strategy for neurodegenerative diseases, Annu. Rev. Pharmacol. Toxicol. 62 (2022) 255–277, https://doi.org/10.1146/ANNUREV-PHARMTOX-052220-103416.

[27] S. Bono, M. Feligioni, M. Corbo, Impaired antioxidant KEAP1-NRF2 system in amyotrophic lateral sclerosis: NRF2 activation as a potential therapeutic strategy, Mol. Neurodegener. 16 (2021), https://doi.org/10.1186/S13024-021-00479-8.

[28] A.I. Rojo, M. Pajares, P. Rada, A. Nuñez, A.J. Nevado-Holgado, R. Killik, F. Van Leuven, E. Ribe, S. Lovestone, M. Yamamoto, A. Cuadrado, NRF2 deficiency replicates transcriptomic changes in Alzheimer's patients and worsens APP and TAU pathology, Redox Biol. 13 (2017) 444–451, https://doi.org/10.1016/j.redox.2017.07.006.

[29] W. Hur, N.S. Gray, Small molecule modulators of antioxidant response pathway, Curr. Opin. Chem. Biol. 15 (2011) 162–173, https://doi.org/10.1016/j.cbpa.2010.12.009.

[30] K. Kanninen, R. Heikkinen, T. Malm, T. Rolova, S. Kuhmonen, H. Leinonen, S. Ylä-Herttuala, H. Tanila, A.L. Levonen, M. Koistinaho, J. Koistinaho, Intrahippocampal injection of a lentiviral vector expressing Nrf2 improves spatial learning in a mouse model of Alzheimer's disease, Proc. Natl. Acad. Sci. U. S. A. 106 (2009) 16505–16510, https://doi.org/10.1073/PNAS.0908397106.

[31] C. Branca, E. Ferreira, T.V. Nguyen, K. Doyle, A. Caccamo, S. Oddo, Genetic reduction of Nrf2 exacerbates cognitive deficits in a mouse model of Alzheimer's disease, Hum. Mol. Genet. 26 (2017) 4823–4835, https://doi.org/10.1093/HMG/DDX361.

[32] A. Faria-Pereira, V.A. Morais, Synapses: the brain's energy-demanding sites, Int. J. Mol. Sci. 23 (2022), https://doi.org/10.3390/IJMS23073627.

[33] S. Rumpf, N. Sanal, M. Marzano, Energy metabolic pathways in neuronal development and function, Oxford Open Neuroscience 2 (2023), https://doi.org/10.1093/OONS/KVAD004.

[34] M.S. Goyal, M.E. Raichle, Glucose requirements of the developing human brain, J. Pediatr. Gastroenterol. Nutr. 66 (2018) S46, https://doi.org/10.1097/MPG.0000000000001875.

[35] P. Andrés-Benito, M. Carmona, M. Jordán, J. Fernández-Irigoyen, E. Santamaría, J.A. Del Rio, I. Ferrer, Host tau genotype specifically designs and regulates tau seeding and spreading and host tau transformation following intrahippocampal injection of identical tau AD inoculum, Int. J. Mol. Sci. 23 (2022), https://doi.org/10.3390/IJMS23020718.

[36] I. Ferrer, P. Andrés-Benito, J. Sala-Jarque, V. Gil, J.A. del Rio, Capacity for seeding and spreading of argyrophilic grain disease in a wild-type murine model; comparisons with primary age-related tauopathy, Front. Mol. Neurosci. 13 (2020), https://doi.org/10.3389/FNMOL.2020.00101.

[37] I. Ferrer, P. Andrés-Benito, M. Carmona, J.A. del Rio, Common and specific marks of different tau strains following intra-hippocampal injection of AD, PiD, and GGT inoculum in hTau transgenic mice, Int. J. Mol. Sci. 23 (2022), https://doi.org/10.3390/IJMS232415940.

[38] I. Ferrer, M.V. Zelaya, M. Aguiló García, M. Carmona, I. López-González, P. Andrés-Benito, L. Lidón, R. Gavín, P. Garcia-Esparcia, J.A. del Rio, Relevance of host tau in tau seeding and spreading in tauopathies, Brain Pathol. 30 (2020) 298–318, https://doi.org/10.1111/bpa.12778.

[39] I. Ferrer, M.A. García, M. Carmona, P. Andrés-Benito, B. Torrejón-Escribano, P. Garcia-Esparcia, J.A. Del Rio, Involvement of oligodendrocytes in tau seeding and spreading in tauopathies, Front. Aging Neurosci. 11 (2019), https://doi.org/10.3389/FNAGI.2019.00112.

[40] S. Sandouka, A. Saadi, P.K. Singh, R. Olowe, T. Shekh-Ahmad, Nrf2 is predominantly expressed in hippocampal neurons in a rat model of temporal lobe epilepsy, Cell Biosci. 13 (2023), https://doi.org/10.1186/S13578-022-00951-Y.

[41] C. Laurent, G. Dorothée, S. Hunot, E. Martin, Y. Monnet, M. Duchamp, Y. Dong, F. P. Légeron, A. Leboucher, S. Burnouf, E. Faivre, K. Carvalho, R. Caillierez, N. Zommer, D. Demeyer, N. Jouy, V. Sazdovitch, S. Schraen-Maschke, C. Delarasse, L. Buée, D. Blum, Hippocampal T cell infiltration promotes neuroinflammation and cognitive decline in a mouse model of tauopathy, Brain 140 (2017) 184–200, https://doi.org/10.1093/BRAIN/AWW270.

[42] I. Ferrer, P. Andrés-Benito, P. Garcia-Esparcia, I. López-Gonzalez, D. Valiente, M. Jordán-Pirla, M. Carmona, J. Sala-Jarque, V. Gil, J.A. Del Rio, Differences in tau seeding in newborn and adult wild-type mice, Int. J. Mol. Sci. 23 (2022), https://doi.org/10.3390/IJMS23094789.

[43] K.B.J. George Paxinos, Franklin, Paxinos and Franklin's the Mouse Brain in Stereotaxic Coordinates, 2019.

[44] I. López-González, E. Aso, M. Carmona, M. Armand-Ugon, R. Blanco, A. Naudí, R. Cabré, M. Portero-Otin, R. Pamplona, I. Ferrer, Neuroinflammatory gene regulation, mitochondrial function, oxidative stress, and brain lipid modifications with disease progression in tau P301S transgenic mice as a model of frontotemporal lobar degeneration-tau, J. Neuropathol. Exp. Neurol. 74 (2015) 975–999, https://doi.org/10.1097/NEN.0000000000000241.

[45] I. López-González, A. Schlüter, E. Aso, P. Garcia-Esparcia, B. Ansoleaga, F. Llorens, M. Carmona, J. Moreno, A. Fuso, M. Portero-Otin, R. Pamplona, A. Pujol, I. Ferrer, Neuroinflammatory signals in alzheimer disease and APP/PS1 transgenic mice: correlations with plaques, tangles, and oligomeric species, J. Neuropathol. Exp. Neurol. 74 (2015) 319–344, https://doi.org/10.1097/NEN.0000000000000176.

[46] P. Andrés-Benito, Á. Flores, S. Busquet-Areny, M. Carmona, K. Ausín, P. Cartas-Cejudo, M. Lachén-Montes, J.A. Del Rio, J. Fernández-Irigoyen, E. Santamaría, I. Ferrer, Deregulated transcription and proteostasis in adult mapt knockout mouse, Int. J. Mol. Sci. 24 (2023), https://doi.org/10.3390/IJMS24076559.

[47] Babraham bioinformatics - FastQC A quality control tool for high throughput sequence data, (n.d.). https://www.bioinformatics.babraham.ac.uk/projects/fastqc/(accessed September 4, 2025).

[48] P. Ewels, M. Magnusson, S. Lundin, M. Käller, MultiQC: summarize analysis results for multiple tools and samples in a single report, Bioinformatics 32 (2016) 3047–3048, https://doi.org/10.1093/BIOINFORMATICS/BTW354.

[49] A. Dobin, C.A. Davis, F. Schlesinger, J. Drenkow, C. Zaleski, S. Jha, P. Batut, M. Chaisson, T.R. Gingeras, STAR: ultrafast universal RNA-seq aligner, Bioinformatics 29 (2013) 15–21, https://doi.org/10.1093/BIOINFORMATICS/BTS635.

[50] H. Li, B. Handsaker, A. Wysoker, T. Fennell, J. Ruan, N. Homer, G. Marth, G. Abecasis, R. Durbin, The sequence alignment/map format and SAMtools, Bioinformatics 25 (2009) 2078–2079, https://doi.org/10.1093/BIOINFORMATICS/BTP352.

[51] GitHub - broadinstitute/picard: A set of command line tools (in Java) for manipulating high-throughput sequencing (HTS) data and formats such as SAM/BAM/CRAM and VCF., (n.d.). https://github.com/broadinstitute/picard (accessed September 4, 2025).

[52] Y. Liao, G.K. Smyth, W. Shi, The R package Rsubread is easier, faster, cheaper and better for alignment and quantification of RNA sequencing reads, Nucleic Acids Res. 47 (2019), https://doi.org/10.1093/NAR/GKZ114.

[53] M.I. Love, W. Huber, S. Anders, Moderated estimation of fold change and dispersion for RNA-seq data with DESeq2, Genome Biol. 15 (2014), https://doi.org/10.1186/S13059-014-0550-8.

[54] S. Durinck, P.T. Spellman, E. Birney, W. Huber, Mapping identifiers for the integration of genomic datasets with the R/bioconductor package biomaRt, Nat. Protoc. 4 (2009) 1184–1191, https://doi.org/10.1038/NPROT.2009.97.

[55] Z. Gu, R. Eils, M. Schlesner, Complex heatmaps reveal patterns and correlations in multidimensional genomic data, Bioinformatics 32 (2016) 2847–2849, https://doi.org/10.1093/BIOINFORMATICS/BTW313.

[56] S.X. Ge, D. Jung, D. Jung, R. Yao, ShinyGO: a graphical gene-set enrichment tool for animals and plants, Bioinformatics 36 (2020) 2628–2629, https://doi.org/10.1093/BIOINFORMATICS/BTZ931.

[57] P. Li, J. Wei, Y. Zhu, CellGO: a novel deep learning-based framework and webserver for cell-type-specific gene function interpretation, Briefings Bioinf. 25 (2024), https://doi.org/10.1093/BIB/BBAD417.

[58] A. Saunders, E.Z. Macosko, A. Wysoker, M. Goldman, F.M. Krienen, H. de Rivera, E. Bien, M. Baum, L. Bortolin, S. Wang, A. Goeva, J. Nemesh, N. Kamitaki, S. Brumbaugh, D. Kulp, S.A. McCarroll, Molecular diversity and specializations among the cells of the adult mouse brain, Cell 174 (2018) 1015–1030.e16, https://doi.org/10.1016/j.cell.2018.07.028.

[59] P. Langfelder, S. Horvath, WGCNA: an R package for weighted correlation network analysis, BMC Bioinf. 9 (2008), https://doi.org/10.1186/1471-2105-9-559.

[60] J.A. Miller, R.L. Woltjer, J.M. Goodenbour, S. Horvath, D.H. Geschwind, Genes and pathways underlying regional and cell type changes in Alzheimer's disease, Genome Med. 5 (2013), https://doi.org/10.1186/GM452.

[61] M.J. Hawrylycz, E.S. Lein, A.L. Guillozet-Bongaarts, E.H. Shen, L. Ng, J.A. Miller, L.N. Van De Lagemaat, K.A. Smith, A. Ebbert, Z.L. Riley, C. Abajian, C. F. Beckmann, A. Bernard, D. Bertagnolli, A.F. Boe, P.M. Cartagena, M. Mallar Chakravarty, M. Chapin, J. Chong, R.A. Dalley, B.D. Daly, C. Dang, S. Datta, N. Dee, T.A. Dolbeare, V. Faber, D. Feng, D.R. Fowler, J. Goldy, B.W. Gregor, Z. Haradon, D.R. Haynor, J.G. Hohmann, S. Horvath, R.E. Howard, A. Jeromin, J. M. Jochim, M. Kinnunen, C. Lau, E.T. Lazarz, C. Lee, T.A. Lemon, L. Li, Y. Li, J. A. Morris, C.C. Overly, P.D. Parker, S.E. Parry, M. Reding, J.J. Royall, J. Schulkin, P.A. Sequeira, C.R. Slaughterbeck, S.C. Smith, A.J. Sodt, S.M. Sunkin, B. E. Swanson, M.P. Vawter, D. Williams, P. Wohnoutka, H. Ronald Zielke, D. H. Geschwind, P.R. Hof, S.M. Smith, C. Koch, S.G.N. Grant, A.R. Jones, An anatomically comprehensive atlas of the adult human brain transcriptome, Nature 489 (2012) 391–399, https://doi.org/10.1038/NATURE11405.

[62] S. Falcon, R. Gentleman, Using GOstats to test gene lists for GO term association, Bioinformatics 23 (2007) 257–258, https://doi.org/10.1093/BIOINFORMATICS/BTL567.

[63] S. Tyanova, T. Temu, P. Sinitcyn, A. Carlson, M.Y. Hein, T. Geiger, M. Mann, J. Cox, The perseus computational platform for comprehensive analysis of (prote) omics data, Nat. Methods 13 (2016) 731–740, https://doi.org/10.1038/nmeth.3901.

[64] A. Martinez-Val, D.B. Bekker-Jensen, S. Steigerwald, C. Koenig, O. Østergaard, A. Mehta, T. Tran, K. Sikorski, E. Torres-Vega, E. Kwasniewicz, S. H. Brynjólfsdóttir, L.B. Frankel, R. Kjøbsted, N. Krogh, A. Lundby, S. Bekker-Jensen, F. Lund-Johansen, J.V. Olsen, Spatial-proteomics reveals phospho-signaling dynamics at subcellular resolution, Nat. Commun. 12 (2021), https://doi.org/10.1038/S41467-021-27398-Y.

[65] S. Okuda, Y. Watanabe, Y. Moriya, S. Kawano, T. Yamamoto, M. Matsumoto, T. Takami, D. Kobayashi, N. Araki, A.C. Yoshizawa, T. Tabata, N. Sugiyama, S. Goto, Y. Ishihama, JPOSTrepo: an international standard data repository for proteomes, Nucleic Acids Res. 45 (2017) D1107–D1111, https://doi.org/10.1093/NAR/GKW1080.

[66] E.S. Nakayasu, M. Gritsenko, P.D. Piehowski, Y. Gao, D.J. Orton, A.A. Schepmoes, T.L. Fillmore, B.I. Frohnert, M. Rewers, J.P. Krischer, C. Ansong, A.M. Suchy-Dicey, C. Evans-Molina, W.J. Qian, B.J.M. Webb-Robertson, T.O. Metz, Tutorial: best practices and considerations for mass-spectrometry-based protein biomarker discovery and validation, Nat. Protoc. 16 (2021) 3737–3760, https://doi.org/10.1038/S41596-021-00566-6.

[67] D. Pascovici, D.C.L. Handler, J.X. Wu, P.A. Haynes, Multiple testing corrections in quantitative proteomics: a useful but blunt tool, Proteomics 16 (2016) 2448–2453, https://doi.org/10.1002/PMIC.201600044.

[68] A. Fuster-Matanzo, F. Hernández, J. Ávila, Tau spreading mechanisms; implications for dysfunctional tauopathies, Int. J. Mol. Sci. 19 (2018) 645, https://doi.org/10.3390/IJMS19030645, 19 (2018) 645.

[69] I. Ferrer, M.A. García, I.L. González, D.D. Lucena, A.R. Villalonga, M.C. Tech, F. Llorens, P. Garcia-Esparcia, A. Martinez-Maldonado, M.F. Mendez, B. T. Escribano, J.J.B. Serra, E. Sabido, C. de la Torre Gómez, J.A. del Rio, Aging-related tau astrogliopathy (ARTAG): not only tau phosphorylation in astrocytes, Brain Pathol. 28 (2018) 965–985, https://doi.org/10.1111/BPA.12593.

[70] A.I. Rojo, M. Pajares, A.J. García-Yagüe, I. Buendia, F. Van Leuven, M. Yamamoto, M.G. López, A. Cuadrado, Deficiency in the transcription factor NRF2 worsens inflammatory parameters in a mouse model with combined tauopathy and amyloidopathy, Redox Biol. 18 (2018) 173–180, https://doi.org/10.1016/j.redox.2018.07.006.

[71] R. Riordan, W. Rong, Z. Yu, G. Ross, J. Valerio, J. Dimas-Muñoz, V. Heredia, K. Magnusson, V. Galvan, V.I. Perez, Effect of Nrf2 loss on senescence and cognition of tau-based P301S mice, GeroScience 45 (2023) 1451–1469, https://doi.org/10.1007/S11357-023-00760-2.

[72] S. Sun, M. Yu, L. Yu, W. Huang, M. Zhu, Y. Fu, L. Yan, Q. Wang, X. Ji, J. Zhao, M. Wu, Nrf2 silencing amplifies DNA photooxidative damage to activate the STING pathway for synergistic tumor immunotherapy, Biomaterials 296 (2023), https://doi.org/10.1016/j.biomaterials.2023.122068.

[73] J.M. Quiles, M. Narasimhan, T. Mosbruger, G. Shanmugam, D. Crossman, N. S. Rajasekaran, Identification of transcriptome signature for myocardial reductive stress, Redox Biol. 13 (2017) 568–580, https://doi.org/10.1016/j.redox.2017.07.013.

[74] A.T. Dinkova-Kostova, R.V. Kostov, A.G. Kazantsev, The role of Nrf2 signaling in counteracting neurodegenerative diseases, FEBS J. 285 (2018) 3576–3590, https://doi.org/10.1111/FEBS.14379.

[75] J.R.C. Priestley, K.E. Kautenburg, M.C. Casati, B.T. Endres, A.M. Geurts, J. H. Lombard, The NRF2 knockout rat: a new animal model to study endothelial dysfunction, oxidant stress, and microvascular rarefaction, Am. J. Physiol. Heart Circ. Physiol. 310 (2016) H478–H487, https://doi.org/10.1152/AJPHEART.00586.2015.

[76] J.M. Quiles, M. Narasimhan, G. Shanmugam, B. Milash, J.R. Hoidal, N. S. Rajasekaran, Differential regulation of miRNA and mRNA expression in the myocardium of Nrf2 knockout mice, BMC Genom. 18 (2017), https://doi.org/10.1186/S12864-017-3875-3.

[77] E.S. Acuner-Ozbabacan, B.H. Engin, E. Guven-Maiorov, G. Kuzu, S. Muratcioglu, A. Baspinar, Z. Chen, C. Van Waes, A. Gursoy, O. Keskin, R. Nussinov, The structural network of Interleukin-10 and its implications in inflammation and cancer, BMC Genom. 15 (2014) S2, https://doi.org/10.1186/1471-2164-15-S4-S2.

[78] A. Yoshimura, Y. Wakabayashi, T. Mori, Cellular and molecular basis for the regulation of inflammation by TGF-β, J. Biochem. 147 (2010) 781–792, https://doi.org/10.1093/JB/MVQ043.

[79] A. Putra, F.B. Ridwan, A.I. Putridewi, A.R. Kustiyah, K. Wirastuti, N.A.C. Sadyah, I. Rosdiana, D. Munir, The role of TNF-α induced MSCs on suppressive inflammation by increasing TGF-β and IL-10, Open Access Maced. J. Med. Sci. 6 (2018) 1779, https://doi.org/10.3889/OAMJMS.2018.404.

[80] J.I. Szu, D.K. Binder, The role of astrocytic aquaporin-4 in synaptic plasticity and learning and memory, Front. Integr. Neurosci. 10 (2016), https://doi.org/10.3389/FNINT.2016.00008.

[81] L.C. Dabin, H. Kersey, B. Kim, D.J. Acri, D. Sharify, A. Lee-Gosselin, C.A. Lasagna-Reeves, A.L. Oblak, B.T. Lamb, J. Kim, Loss of Inpp5d has disease-relevant and sex-specific effects on glial transcriptomes, Alzheimer's Dement. 20 (2024) 5311–5323, https://doi.org/10.1002/ALZ.13901.

[82] H. Zhang, X. Zhang, Y. Chai, Y. Wang, J. Zhang, X. Chen, Astrocyte-mediated inflammatory responses in traumatic brain injury: mechanisms and potential interventions, Front. Immunol. 16 (2025), https://doi.org/10.3389/FIMMU.2025.1584577.

[83] P. Nardin, F. Tramontina, M.C. Leite, A.C. Tramontina, A. Quincozes-Santos, L.M. V. de Almeida, A.M. Battastini, C. Gottfried, C.A. Gonçalves, S100B content and secretion decrease in astrocytes cultured in high-glucose medium, Neurochem. Int. 50 (2007) 774–782, https://doi.org/10.1016/j.neuint.2007.01.013.

[84] M.F. McDermott, I. Aksentijevich, J. Galon, E.M. McDermott, B. William Ogunkolade, M. Centola, E. Mansfield, M. Gadina, L. Karenko, T. Pettersson, J. McCarthy, D.M. Frucht, M. Aringer, Y. Torosyan, A.M. Teppo, M. Wilson, H. Mehmet Karaarslan, Y. Wan, L. Todd, G. Wood, R. Schlimgen, T. R. Kumarajeewa, S.M. Cooper, J.P. Vella, C.I. Amos, J. Mulley, K.A. Quane, M. G. Molloy, A. Ranki, R.J. Powell, G.A. Hitman, J.J. O'Shea, D.L. Kastner, Germline mutations in the extracellular domains of the 55 kDa TNF receptor, TNFR1, define a family of dominantly inherited autoinflammatory syndromes, Cell 97 (1999) 133–144, https://doi.org/10.1016/S0092-8674(00)80721-7.

[85] H. Wajant, K. Pfizenmaier, P. Scheurich, Tumor necrosis factor signaling, Cell Death Differ. 10 (2003) 45–65, https://doi.org/10.1038/SJ.CDD.4401189.

[86] M.O. Li, R.A. Flavell, TGF-β: a master of all T cell trades, Cell 134 (2008) 392–404, https://doi.org/10.1016/j.cell.2008.07.025.

[87] D. Peng, M. Fu, M. Wang, Y. Wei, X. Wei, Targeting TGF-β signal transduction for fibrosis and cancer therapy, Mol. Cancer 21 (2022), https://doi.org/10.1186/S12943-022-01569-X.

[88] E.-O. Glocker, D. Kotlarz, K. Boztug, E.M. Gertz, A.A. Schäffer, F. Noyan, M. Perro, J. Diestelhorst, A. Allroth, D. Murugan, N. Hätscher, D. Pfeifer, K.-W. Sykora, M. Sauer, H. Kreipe, M. Lacher, R. Nustede, C. Woellner, U. Baumann, U. Salzer, S. Koletzko, N. Shah, A.W. Segal, A. Sauerbrey, S. Buderus, S. B. Snapper, B. Grimbacher, C. Klein, Inflammatory bowel disease and mutations affecting the Interleukin-10 receptor, N. Engl. J. Med. 361 (2009) 2033–2045, https://doi.org/10.1056/NEJMOA0907206.

[89] P.J. Murray, Understanding and exploiting the endogenous interleukin-10/STAT3-mediated anti-inflammatory response, Curr. Opin. Pharmacol. 6 (2006) 379–386, https://doi.org/10.1016/j.coph.2006.01.010.

[90] C. Jo, S. Gundemir, S. Pritchard, Y.N. Jin, I. Rahman, G.V.W. Johnson, Nrf2 reduces levels of phosphorylated tau protein by inducing autophagy adaptor protein NDP52, Nat. Commun. 5 (2014), https://doi.org/10.1038/NCOMMS4496.

[91] Y. Xu, S. Zhang, H. Zheng, The cargo receptor SQSTM1 ameliorates neurofibrillary tangle pathology and spreading through selective targeting of pathological MAPT (microtubule associated protein tau), Autophagy 15 (2019) 583–598, https://doi.org/10.1080/15548627.2018.1532258.

[92] C.A. Piantadosi, H.B. Suliman, Redox regulation of mitochondrial biogenesis, Free Radic. Biol. Med. 53 (2012) 2043, https://doi.org/10.1016/J.FREERADBIOMED.2012.09.014.

[93] M. Puchades, C.J. Sogn, J. Maehlen, L.H. Bergersen, V. Gundersen, Unaltered lactate and glucose transporter levels in the MPTP mouse model of Parkinson's disease, J. Parkinsons Dis. 3 (2013) 371–385, https://doi.org/10.3233/JPD-130190.

[94] N. Esteras, T.S. Blacker, E.A. Zherebtsov, O.A. Stelmashuk, Y. Zhang, W. C. Wigley, M.R. Duchen, A.T. Dinkova-Kostova, A.Y. Abramov, Nrf2 regulates glucose uptake and metabolism in neurons and astrocytes, Redox Biol. 62 (2023), https://doi.org/10.1016/j.redox.2023.102672.

[95] R.S. Sohal, R. Weindruch, Oxidative stress, caloric restriction, and aging, Science 273 (1979) 59–63, https://doi.org/10.1126/SCIENCE.273.5271.59;WEBSITE:WEBSITE:AAAS-SITE;JOURNAL:JOURNAL:SCIENCE;WGROUP:STRING:PUBLICATION, 1996.

[96] I. López-González, R. Viana, P. Sanz, I. Ferrer, Inflammation in Lafora disease: evolution with disease progression in laforin and Malin knock-out mouse models, Mol. Neurobiol. 54 (2017) 3119–3130, https://doi.org/10.1007/S12035-016-9884-4.

[97] L. Gao, V. Kumar, N.N. Vellichirammal, S.Y. Park, T.L. Rudebush, L. Yu, W. M. Son, E.J. Pekas, A.M. Wafi, J. Hong, P. Xiao, C. Guda, H.J. Wang, H.D. Schultz, I.H. Zucker, Functional, proteomic and bioinformatic analyses of Nrf2- and Keap1- null skeletal muscle, J. Physiol. (Paris) 598 (2020) 5427–5451, https://doi.org/10.1113/JP280176.

[98] S. Kovac, P.R. Angelova, K.M. Holmström, Y. Zhang, A.T. Dinkova-Kostova, A. Y. Abramov, Nrf2 regulates ROS production by mitochondria and NADPH oxidase, Biochim. Biophys. Acta Gen. Subj. 1850 (2015) 794–801, https://doi.org/10.1016/j.bbagen.2014.11.021.

[99] K.N. Amin, P. Rajaguru, T. Suzuki, K. Sarkar, K. Ganesan, K.M. Ramkumar, Quantitative proteomic analyses uncover regulatory roles of Nrf2 in human endothelial cells, Cell Stress Chaperones 28 (2023) 731–747, https://doi.org/10.1007/S12192-023-01366-5.

[100] W. Kamphuis, C. Mamber, M. Moeton, L. Kooijman, J.A. Sluijs, A.H.P. Jansen, M. Verveer, L.R. de Groot, V.D. Smith, S. Rangarajan, J.J. Rodríguez, M. Orre, E. M. Hol, GFAP isoforms in adult mouse brain with a focus on neurogenic astrocytes and reactive astrogliosis in mouse models of alzheimer disease, PLoS One 7 (2012) e42823, https://doi.org/10.1371/JOURNAL.PONE.0042823.

[101] E.M. Hol, M. Pekny, Glial fibrillary acidic protein (GFAP) and the astrocyte intermediate filament system in diseases of the central nervous system, Curr. Opin. Cell Biol. 32 (2015) 121–130, https://doi.org/10.1016/J.CEB.2015.02.004.

[102] Z. Yang, K.K.W. Wang, Glial Fibrillary acidic protein: from intermediate filament assembly and gliosis to neurobiomarker, Trends Neurosci. 38 (2015) 364, https://doi.org/10.1016/J.TINS.2015.04.003.

[103] C. Escartin, E. Galea, A. Lakatos, J.P. O'Callaghan, G.C. Petzold, A. Serrano-Pozo, C. Steinhäuser, A. Volterra, G. Carmignoto, A. Agarwal, N.J. Allen, A. Araque, L. Barbeito, A. Barzilai, D.E. Bergles, G. Bonvento, A.M. Butt, W.T. Chen, M. Cohen-Salmon, C. Cunningham, B. Deneen, B. De Strooper, B. Díaz-Castro, C. Farina, M. Freeman, V. Gallo, J.E. Goldman, S.A. Goldman, M. Götz, A. Gutiérrez, P.G. Haydon, D.H. Heiland, E.M. Hol, M.G. Holt, M. Iino, K. V. Kastanenka, H. Kettenmann, B.S. Khakh, S. Koizumi, C.J. Lee, S.A. Liddelow, B. A. MacVicar, P. Magistretti, A. Messing, A. Mishra, A.V. Molofsky, K.K. Murai, C. M. Norris, S. Okada, S.H.R. Oliet, J.F. Oliveira, A. Panatier, V. Parpura, M. Pekna, M. Pekny, L. Pellerin, G. Perea, B.G. Pérez-Nievas, F.W. Pfrieger, K.E. Poskanzer, F.J. Quintana, R.M. Ransohoff, M. Riquelme-Perez, S. Robel, C.R. Rose, J. D. Rothstein, N. Rouach, D.H. Rowitch, A. Semyanov, S. Sirko, H. Sontheimer, R. A. Swanson, J. Vitorica, I.B. Wanner, L.B. Wood, J. Wu, B. Zheng, E.R. Zimmer, R. Zorec, M.V. Sofroniew, A. Verkhratsky, Reactive astrocyte nomenclature, definitions, and future directions, Nat. Neurosci. 24 (3 24) (2021) 312–325, https://doi.org/10.1038/s41593-020-00783-4, 2021.

[104] A. Verkhratsky, M. Nedergaard, Physiology of Astroglia, Physiol. Rev. 98 (2018) 239–389, https://doi.org/10.1152/PHYSREV.00042.2016.

[105] E.A. Lepekhin, C. Eliasson, C.H. Berthold, V. Berezin, E. Bock, M. Pekny, Intermediate filaments regulate astrocyte motility, J. Neurochem. 79 (2001) 617–625, https://doi.org/10.1046/J.1471-4159.2001.00595.X.

[106] C. Mamber, W. Kamphuis, N.L. Haring, N. Peprah, J. Middeldorp, E.M. Hol, GFAPδ expression in glia of the developmental and Adolescent mouse brain, PLoS One 7 (2012), https://doi.org/10.1371/JOURNAL.PONE.0052659.

[107] E. Kirsch, N. Szejko, G.J. Falcone, Genetic underpinnings of cerebral edema in acute brain injury: an opportunity for pathway discovery, Neurosci. Lett. 730 (2020), https://doi.org/10.1016/j.neulet.2020.135046.

[108] J. Kim, I.D. Yoo, J. Lim, J.S. Moon, Pathological phenotypes of astrocytes in Alzheimer's disease, Exp. Mol. Med. 56 (2024) 95–99, https://doi.org/10.1038/S12276-023-01148-0;TECHMETA=13,38,39,51;SUBJMETA=340,378,631,87;KWRD=CELLULAR+NEUROSCIENCE,MOLECULAR+NEUROSCIENCE.

[109] L. Liu, M.G. Kelly, X.R. Yang, T.G. Fernandez, E.L. Wierzbicki, A. Skrobach, S. Doré, Nrf2 deficiency exacerbates cognitive impairment and reactive microgliosis in a lipopolysaccharide-induced neuroinflammatory mouse model, Cell. Mol. Neurobiol. 40 (2020) 1185, https://doi.org/10.1007/S10571-020-00807-4.

[110] P. Rawat, U. Sehar, J. Bisht, A. Selman, J. Culberson, P.H. Reddy, Phosphorylated Tau in alzheimer's disease and other tauopathies, Int. J. Mol. Sci. 23 (2022) 12841, https://doi.org/10.3390/IJMS232112841.

[111] N.N. Naseri, H. Wang, J. Guo, M. Sharma, W. Luo, The complexity of tau in Alzheimer's disease, Neurosci. Lett. 705 (2019) 183–194, https://doi.org/10.1016/J.NEULET.2019.04.022.

[112] S. Bachmann, M. Bell, J. Klimek, H. Zempel, Differential effects of the six human TAU isoforms: somatic retention of 2N-TAU and increased microtubule number induced by 4R-TAU, Front. Neurosci. 15 (2021), https://doi.org/10.3389/FNINS.2021.643115.

[113] K.S. Kosik, L.D. Orecchio, S. Bakalis, R.L. Neve, Developmentally regulated expression of specific tau sequences, Neuron 2 (1989) 1389–1397, https://doi.org/10.1016/0896-6273(89)90077-9.

[114] A. Andreadis, Tau gene alternative splicing: expression patterns, regulation and modulation of function in normal brain and neurodegenerative diseases, Biochim. Biophys. Acta Mol. Basis Dis. 1739 (2005) 91–103, https://doi.org/10.1016/j.bbadis.2004.08.010.

[115] J. Avila, E.G. de Barreda, N. Pallas-Bazarra, F. Hernandez, Tau and Neuron aging, Aging Dis 4 (2012) 23. https://pmc.ncbi.nlm.nih.gov/articles/PMC3570138/. (Accessed 27 August 2025).

[116] S. Chen, K. Townsend, T.E. Goldberg, P. Davies, C. Conejero-Goldberg, MAPT isoforms: differential transcriptional profiles related to 3R and 4R splice variants, J. Alzheimers Dis. 22 (2010) 1313, https://doi.org/10.3233/JAD-2010-101155.

[117] I. Lastres-Becker, N.G. Innamorato, T. Jaworski, A. Rábano, S. Kügler, F. Van Leuven, A. Cuadrado, Fractalkine activates NRF2/NFE2L2 and heme oxygenase 1 to restrain tauopathy-induced microgliosis, Brain 137 (2014) 78–91, https://doi.org/10.1093/BRAIN/AWT323.

[118] N. Robledinos-Antón, A.I. Rojo, E. Ferreiro, Á. Núñez, K.H. Krause, V. Jaquet, A. Cuadrado, Transcription factor NRF2 controls the fate of neural stem cells in the subgranular zone of the hippocampus, Redox Biol. 13 (2017) 393–401, https://doi.org/10.1016/j.redox.2017.06.010.